International Journal of Structural Stability and Dynamics
Vol. 18, No. 10 (2018) 1850121 (35 pages)
© World Scientific Publishing Company
DOI: 10.1142/S0219455418501213

A Meshfree Higher Order Mass Matrix Formulation for Structural Vibration Analysis

Junchao Wu*, Dongdong Wang*,‡ and Zeng Lin*,†

*Department of Civil Engineering and
Xiamen Engineering Technology Center
for Intelligent Maintenance of Infrastructures
Xiamen University
Xiamen, Fujian 361005, P. R. China

†School of Mathematical Sciences
Xiamen University
Xiamen, Fujian 361005, P. R. China
‡ddwang@xmu.edu.cn

Received 9 November 2017
Accepted 9 March 2018
Published 16 April 2018

An accurate meshfree formulation with higher order mass matrix is proposed for the structural vibration analysis with particular reference to the 1D rod and 2D membrane problems. Unlike the finite element analysis with an explicit mass matrix, the mass matrix of Galerkin meshfree formulation usually does not have an explicit expression due to the rational nature of meshfree shape functions. In order to develop a meshfree higher order mass matrix, a frequency error measure is derived by using the entries of general symmetric stiffness and mass matrices. The frequency error is then expressed as a series expansion of the nodal distance, in which the coefficients of each term are related to the meshfree stiffness and mass matrices. It is theoretically proved that the constant coefficient in the frequency error vanishes identically provided with the linear completeness condition, which does not rely on any specific form of the shape functions. Furthermore, a meshfree higher order mass matrix is developed through a linear combination of the consistent and lumped mass matrices, in which the optimal mass combination coefficient is attained via eliminating the lower order error terms. In particular, the proposed higher order mass matrix with Galerkin meshfree formulation achieves a fourth-order accuracy when the moving least squares or reproducing kernel (RK) meshfree approximation with linear basis function is employed; nonetheless, the conventional meshfree method only gives a second-order accuracy for the frequency computation. In the multidimensional formulation, the optimal mass combination coefficient is a function of the wave propagation angle so that the proposed accurate meshfree method is applicable to the computation of frequencies associated with any wave propagation direction. The superconvergence of the proposed meshfree higher order mass matrix formulation is validated via numerical examples.

Keywords: Meshfree method; free vibration; frequency analysis; meshfree higher order mass matrix; superconvergence.

‡Corresponding author.

1. Introduction

The frequency computation is an essential ingredient of structural vibration analysis. Nowadays, numerical methods have been widely used in frequency computation, for example, the finite element methods[1] and boundary element methods.[2] Alternatively, the meshfree methods featured by point- or particle-based approximations[3–17] relieve the mesh requirements of finite elements and provide a very useful tool for structural dynamics analysis. For example, the RK particle method for dynamic analysis was presented by Liu *et al.*[18] and Chen *et al.*[6] A radial point interpolation method was proposed by Liu and Gu[19] for free vibration analysis. Zhou *et al.*[20] elaborated the free and forced vibration analysis with RK particle method. Chen *et al.*[21] and Liu *et al.*[22] employed the meshless radial basis function for free vibration and buckling analysis of plates. A Hermite RK Galerkin meshfree method with subdomain stabilized conforming integration (SSCI) was introduced by Wang and Lin[23] for thin plate vibration analysis. Bui *et al.*[24] studied structural dynamic analysis with a moving Kriging interpolation-based element-free Galerkin method. The Galerkin meshfree free vibration analysis of corrugated-core sandwich plates was discussed by Peng *et al.*[25] Zhang *et al.*[26] presented a quasi-convex coupled isogeometric-meshfree method for the free vibration analysis of cracked thin plates. Soltanimaleki *et al.*[27] performed a three-dimensional meshfree free vibration analysis of functionally graded fiber-reinforced cylindrical panels, among many others. The dispersion characteristics of Galerkin meshfree methods were studied by Christon and Voth,[28] You *et al.*,[29] Wang and Lin,[30,31] and so on. The meshfree mass matrices employed in the aforementioned works mainly refer to either consistent or lumped mass matrices.

It is well recognized in the finite element analysis that a higher order mass matrix leads to much more favorable frequency accuracy in contrast to the consistent and lumped mass matrices. Quite often, the higher order mass matrix is built as a linear combination of the consistent and lumped mass matrices through the mass combination parameter.[32–38] However, this may not always be the case. For example, for the isogeometric analysis with higher order smoothing basis functions, a reduced bandwidth mass matrix and its combination with the consistent mass matrix are proposed by Wang *et al.*[39,40] to develop the corresponding higher order mass matrix. In the meantime, for higher order finite elements, the Lagrangian type of Lobatto elements that take the Lobatto points as nodes is preferred to uniformly constructed higher order mass matrices.[38] Furthermore, in order to resolve the wave propagation directional dependence issue for multidimensional higher order mass matrices, the optimal mass combination parameter can be designed as a function of the wave propagation angle,[41,42] or a set of quadrature rules can be devised to formulate the mass and stiffness matrices.[43] It is noted that these developments particularly rely on the explicit structure of the finite element or isogeometric mass and stiffness matrices. A direct generalization of the finite element higher order mass matrix formulation to meshfree methods faces a severe difficulty regarding the nonexplicit mass

and stiffness entries, resulting from the rational shape functions and adjustable nodal influence domains.

This study aims to develop a meshfree higher order mass matrix formulation for accurate structural vibration analysis, with particular reference to the moving least squares/RK (MLS/RK) meshfree formulation with linear basis function. In this present development, a linear combination of the consistent and lumped meshfree mass matrices is utilized as the foundation to derive the higher order mass matrix. A frequency error expression is derived under the harmonic wave assumption. This frequency error expression is quite general and not necessary to restore to the explicit entries of the mass and stiffness matrices. Meanwhile, a set of conditions corresponding to different orders of accuracy is rationally deduced. Subsequently, several properties associated with mass and stiffness matrices are proved based on the linear consistency condition, which ensures a second order of accuracy for the consistent mass matrix formulation. It is also noted that these properties do not rely on the explicit mass and stiffness matrix entries. Further enforcing the vanishment condition of the second-order error term thus gives a meshfree higher order mass formulation with an optimal mass combination parameter. Both one-dimensional (1D) and two-dimensional (2D) cases are discussed. In the two-dimensional case, the wave propagation angle is incorporated into the optimal mass combination parameter in order to remove the wave propagation directional dependence problem regarding the frequency accuracy.

The remainder of this paper is organized as follows. The MLS/RK meshfree approximation and the discrete meshfree equations for structural vibration analysis are outlined in Sec. 2, in which the domain integration using the efficient sub-domain stabilized conforming nodal integration (SCNI) is also briefed. In Sec. 3, a general frequency error expression is first presented and consequently 1D and 2D meshfree higher order mass matrices are established in a sequence. Numerical results are given in Sec. 4 to validate the proposed meshfree higher order mass matrix formulation. Finally, concluding remarks are drawn in Sec. 5.

2. Galerkin Meshfree Formulation for Free Vibration Analysis

2.1. *Meshfree approximation*

In meshfree approximation, a problem domain Ω with boundary Γ is discretized by a group of nodes or particles $\mathbf{x}_I$'s, $I = 1, \ldots, NP$. Each meshfree node is equipped with a shape function $\Psi_I(\mathbf{x})$ which has a local influence domain denoted by $\text{supp}(\mathbf{x}_I)$. According to MLS/RK approximation,[3–6] a meshfree approximant of a scalar field variable $u(\mathbf{x})$, denoted by $u^h(\mathbf{x})$, can be expressed as:

$$u^h(\mathbf{x}) = \sum_{I \in \mathcal{G}_I} \Psi_I(\mathbf{x}) d_I, \tag{1}$$

where the node number set $\mathcal{G}_I$ is defined as $\mathcal{G}_I = \{I | \mathbf{x} \in \text{supp}(\mathbf{x}_I)\}$, d_I is the nodal coefficient associated with the node $\mathbf{x}_I$. $\Psi_I(\mathbf{x})$ is the MLS/RK meshfree shape

function that takes the following form:

$$\Psi_I(\mathbf{x}) = \mathbf{p}^T(\mathbf{x}_I - \mathbf{x})\mathbf{c}(\mathbf{x})\phi_{s_I}(\mathbf{x}_I - \mathbf{x}), \tag{2}$$

in which $\phi_{s_I}(\mathbf{x}_I - \mathbf{x})$ is the non-negative kernel function located at $\mathbf{x}_I$. $\phi_{s_I}(\mathbf{x}_I - \mathbf{x})$ has a support size "s_I" that defines the local influence domain $\text{supp}(\mathbf{x}_I)$. The cubic B-spline function[6] is used as the kernel function herein. $\mathbf{p}(\mathbf{x})$ is the nth order monomial basis vector:

$$\mathbf{p}(\mathbf{x}) = \{1, x, y, x^2, xy, y^2, \ldots, x^i y^j, \ldots, y^n\}^T, \quad i + j \leq n. \tag{3}$$

The unknown vector $\mathbf{c}(\mathbf{x})$ in Eq. (3) can be attained through imposing the so-called nth order consistency conditions[5,6]:

$$\sum_{I \in \mathcal{G}_I} \Psi_I(\mathbf{x})\mathbf{p}(\mathbf{x}_I) = \mathbf{p}(\mathbf{x}) \tag{4}$$

or equivalently,

$$\sum_{I \in \mathcal{G}_I} \Psi_I(\mathbf{x})\mathbf{p}(\mathbf{x}_I - \mathbf{x}) = \mathbf{p}(\mathbf{0}). \tag{5}$$

Substituting Eq. (2) into Eq. (5) immediately gives:

$$\mathbf{A}(\mathbf{x})\mathbf{c}(\mathbf{x}) = \mathbf{p}(\mathbf{0}), \tag{6}$$

where $\mathbf{A}(\mathbf{x})$ is the moment matrix:

$$\mathbf{A}(\mathbf{x}) = \sum_{I \in \mathcal{G}_I} \mathbf{p}(\mathbf{x}_I - \mathbf{x})\mathbf{p}^T(\mathbf{x}_I - \mathbf{x})\phi_{s_I}(\mathbf{x}_I - \mathbf{x}). \tag{7}$$

Consequently, we arrive at $\mathbf{c}(\mathbf{x}) = \mathbf{A}^{-1}(\mathbf{x})\mathbf{p}(\mathbf{0})$ from Eq. (6), and the meshfree shape function of Eq. (7) eventually becomes:

$$\Psi_I(\mathbf{x}) = \mathbf{p}^T(\mathbf{0})\mathbf{A}^{-1}(\mathbf{x})\mathbf{p}(\mathbf{x}_I - \mathbf{x})\phi_{s_I}(\mathbf{x}_I - \mathbf{x}). \tag{8}$$

2.2. *Galerkin meshfree equations*

In this study, we consider the following classical wave equation that governs the 1D rod and 2D membrane vibrations:

$$\ddot{u}(\mathbf{x}, t) = c^2 \nabla^2 u(\mathbf{x}, t), \tag{9}$$

where $u(\mathbf{x}, t)$ stands for the field variable, for instance, the longitudinal displacement of 1D rod or transverse deflection of 2D membrane structures. ∇^2 is the Laplace operator, t denotes time and c is the wave speed. According to the standard harmonic wave assumption, the field variable $u(\mathbf{x}, t)$ can be expressed as:

$$u(\mathbf{x}, t) = u_0 \exp[\iota(\mathbf{k} \cdot \mathbf{x} - \omega t)], \quad \iota = \sqrt{-1}, \tag{10}$$

where u_0 denotes the wave amplitude, $\mathbf{k} = \{k_x, k_y\}^T$, k_x and k_y represent the wave numbers in x and y directions, respectively. ω is the continuum angular frequency.

Substituting Eq. (10) into (9) yields:

$$\omega = ck = c\sqrt{k_x^2 + k_y^2}, \quad k = \sqrt{k_x^2 + k_y^2}. \tag{11}$$

The Galerkin meshfree analysis corresponding to the weak form of Eq. (9) takes the following form:

$$\int_\Omega \delta u \ddot{u} d\Omega + c^2 \int_\Omega \nabla \delta u \cdot \nabla u d\Omega = 0, \tag{12}$$

in which ∇ is the gradient operator. Within the Bubnov–Galerkin context, introducing the meshfree field variable approximation of Eq. (1) into the weak form of Eq. (12) gives the following meshfree discrete equation for free vibration analysis:

$$\mathbf{M}\ddot{\mathbf{d}} + c^2\mathbf{K}\mathbf{d} = \mathbf{0}, \tag{13}$$

where $\mathbf{d}$ is the vector containing the nodal coefficients. $\mathbf{M}$ and $\mathbf{K}$ are the consistent mass matrix and stiffness matrix and their corresponding entries are given by:

$$M_{IJ} = \int_\Omega \Psi_I(\mathbf{x})\Psi_J(\mathbf{x}) d\Omega, \tag{14}$$

$$K_{IJ} = \int_\Omega [\nabla \Psi_I(\mathbf{x})] \cdot [\nabla \Psi_J(\mathbf{x})] d\Omega. \tag{15}$$

It is noted that a lumped mass matrix $\mathbf{M}^l$ with diagonal components only is often used in structural vibration analysis. One straightforward way to compute the component M_{IJ}^l of the lumped mass matrix $\mathbf{M}^l$ is to perform the row-summing on the consistent mass matrix $\mathbf{M}$:

$$M_{IJ}^l = \delta_{IJ} \sum_{K \in \mathcal{S}_{KI}} M_{IK} = \delta_{IJ} \int_\Omega \Psi_I(\mathbf{x}) d\Omega \quad \text{(on sum on } I\text{)}, \tag{16}$$

where the node number set $\mathcal{S}_{KI}$ is defined as $\mathcal{S}_{KI} = \{K | \text{supp}(\mathbf{x}_K) \cap \text{supp}(\mathbf{x}_I) \neq \emptyset\}$. δ_{IJ} stands for the Kronecker delta.

Moreover, a discrete harmonic representation of the vector $\mathbf{d}$ takes the form of $\mathbf{d}(t) = \boldsymbol{\phi} \exp(\iota \omega^h t)$, where ω^h is the semi-discrete frequency and $\boldsymbol{\phi}$ is the corresponding mode. Subsequently bringing the discrete harmonic representation of $\mathbf{d}$ into Eq. (13) produces the standard generalized eigenvalue problem:

$$c^2\mathbf{K}\boldsymbol{\phi} = (\omega^h)^2\mathbf{M}\boldsymbol{\phi}. \tag{17}$$

In this study, we would like to propose an accurate way to compute the frequency ω^h in the category of meshfree method.

2.3. *Numerical integration for stiffness and mass matrices*

Due to the rational nature and the influence domain overlapping characteristics of the MLS/RK meshfree shape functions, efficient and accurate integration of the

Galerkin weak form has been an important topic for meshfree methods and many approaches have been proposed for the meshfree stiffness integration.[44–56] Among the different methods, the strain smoothing-based SCNI proposed by Chen *et al.*[45] ensures the linear exactness of Galerkin formulation and has undergone substantial subsequent developments,[47–56] for example, the SSCI.[23,48–50] In the structural vibration analysis considered herein, the integration of both mass and stiffness matrices should be properly taken into account. It is noted that although SCNI can be adopted to efficiently integrate the stiffness matrix, it is not sufficient to properly integrate the mass matrix due to the order difference between the meshfree shape functions and their derivatives appeared in the mass and stiffness matrices.[29]

In this work, to facilitate the numerical implementation, the method of SSCI[23,48–50] is employed to simultaneously formulate the mass and stiffness matrices. In SSCI, the problem domain Ω is partitioned into a set of integration cells Ω_C's, $C = 1, 2, \ldots, \text{NIC}$, i.e. $\Omega = \cup_{C=1}^{\text{NIC}}(\Omega_C)$, and each cell Ω_C is further sub-divided into sub-domains Ω_C^Ss, $S = 1, 2, \ldots, \text{NS}$ in each direction. Here two sub-domains in each direction, i.e. $\text{NS} = 2$, are adopted. Consider the schematic description of SSCI in Fig. 1, the stiffness matrix component K_{IJ} is computed as follows:

$$K_{IJ} = \sum_{C=1}^{\text{NIC}} \sum_{S=1}^{\text{NS}} [\tilde{\nabla}\Psi_I(\mathbf{x}_C^S)] \cdot [\tilde{\nabla}\Psi_J(\mathbf{x}_C^S)] A_C^S, \tag{18}$$

where $\mathbf{x}_C^S$ is the sampling integration point, i.e. the centroid of the sub-domain Ω_C^S. $\tilde{\nabla}\Psi_I(\mathbf{x}_C^S)$ is the smoothed gradient defined in the sub-domain Ω_C^S:

$$\tilde{\nabla}\Psi_I(\mathbf{x}_C^S) = \frac{1}{A_C^S} \int_{\Gamma_C^S} \Psi_I(\mathbf{x}_C^S)\mathbf{n} d\Gamma, \tag{19}$$

in which Γ_C^S and A_C^S denote the boundary and area of Ω_C^S, respectively. $\mathbf{n}$ stands for the outward normal of Γ_C^S. Using the same set of sampling integration points, the

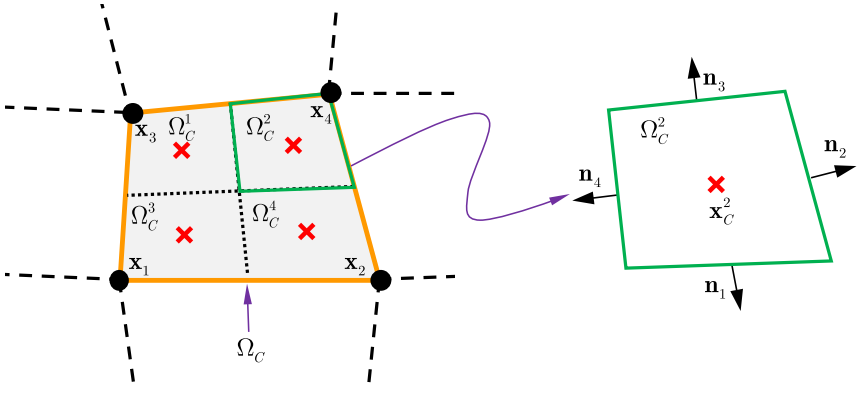

Fig. 1. Schematic illustration of SSCI.

consistent mass matrix component is evaluated as:

$$M_{IJ} = \sum_{C=1}^{\text{NIC}} \sum_{S=1}^{\text{NS}} \Psi_I(\mathbf{x}_C^S)\Psi_J(\mathbf{x}_C^S)A_C^S. \tag{20}$$

3. Meshfree Higher Order Mass Matrix Formulation

3.1. *1D meshfree higher order mass matrix*

Herein the meshfree higher order mass matrix is built upon the following mixed mass matrix $\mathbf{M}^m$ via a linear combination of the consistent and lumped mass matrices[35,39]:

$$M_{IJ}^m(\gamma) = (1-\gamma)M_{IJ}^l + \gamma M_{IJ}, \tag{21}$$

where γ is the mass combination parameter. Replacing the consistent mass matrix $\mathbf{M}$ with the mixed mass matrix $\mathbf{M}^m$ in the equation of motion defined by Eq. (13) yields the following stencil equation associated with a generic node or particle x_I:

$$\sum_{J\in\mathcal{S}_{JI}} M_{IJ}^m \ddot{d}_J + c^2 \sum_{J\in\mathcal{S}_{JI}} K_{IJ} d_J = 0. \tag{22}$$

Meanwhile, a discrete harmonic wave related to a generic node x_J takes the following form:

$$\begin{cases} d_J(x,t) = d_0 \exp[\iota(kx_J - \omega^h t)] \\ \ddot{d}_J(x,t) = -(\omega^h)^2 d_J(x,t) \end{cases}. \tag{23}$$

It is also noted that the common uniform discretization assumption is adopted throughout the subsequent analytical developments.

Substituting Eq. (23) into Eq. (22) yields the following semi-discrete equation:

$$-(\omega^h)^2 \sum_{J\in\mathcal{S}_{JI}} M_{IJ}^m d_J + c^2 \sum_{J\in\mathcal{S}_{JI}} K_{IJ} d_J = 0. \tag{24}$$

Therefore ω^h can be attained as:

$$\begin{aligned} \frac{\omega^h}{\omega} &= \frac{1}{k}\sqrt{\frac{\sum_{J\in\mathcal{S}_{JI}} K_{IJ} d_J}{\sum_{J\in\mathcal{S}_{JI}} M_{IJ}^m d_J}} = \sqrt{\frac{(kh)^{-2}\sum_{J\in\mathcal{S}_{JI}} K_{IJ} h d_J}{\sum_{J\in\mathcal{S}_{JI}} M_{IJ}^m h^{-1} d_J}} \\ &= \sqrt{\frac{(kh)^{-2}\sum_{J\in\mathcal{S}_{JI}} K_{IJ} h \exp[\iota k(x_J - x_I)]}{\sum_{J\in\mathcal{S}_{JI}} M_{IJ}^m h^{-1} \exp[\iota k(x_J - x_I)]}} \\ &= \sqrt{\frac{(kh)^{-2}\sum_{J\in\mathcal{S}_{JI}} K_{IJ} h \exp(\iota k \Delta_{IJ} h)}{\sum_{J\in\mathcal{S}_{JI}} M_{IJ}^m h^{-1} \exp(\iota k \Delta_{IJ} h)}}, \end{aligned} \tag{25}$$

where we have used the continuum frequency ω defined by Eq. (11). As shown in Fig. 2, h is the length between two neighboring meshfree nodes. Δ_{IJ} is a parameter that describes the relative or normalized distance between nodes x_I and x_J, and it is

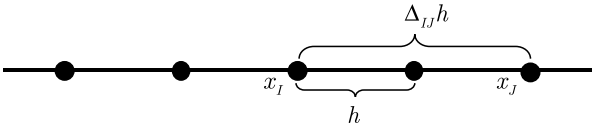

Fig. 2. Schematic illustration of 1D meshfree discretization.

independent of the nodal distance h:

$$\Delta_{IJ} = \frac{x_J - x_I}{h}. \tag{26}$$

After employing the Taylor's expansion, Eq. (25) reduces to:

$$\frac{\omega^h}{\omega} = \sqrt{\frac{\vartheta}{\ell}} \approx 1 + \frac{\vartheta - \ell}{2\vartheta}, \tag{27}$$

where ϑ and ℓ are given by:

$$\begin{aligned}\vartheta &= \frac{1}{(kh)^2} \sum_{J \in \mathcal{S}_{JI}} K_{IJ} h \exp(\iota k \Delta_{IJ} h) \\ &\approx \frac{1}{(kh)^2} \sum_{J \in \mathcal{S}_{JI}} K_{IJ} h \bigg[1 + \iota \Delta_{IJ} kh - \frac{1}{2!}\Delta_{IJ}^2 (kh)^2 - \frac{1}{3!}\iota \Delta_{IJ}^3 (kh)^3 \\ &\quad + \frac{1}{4!}\Delta_{IJ}^4 (kh)^4 + \cdots \bigg], \end{aligned} \tag{28}$$

$$\begin{aligned}\ell &= \sum_{J \in \mathcal{S}_{JI}} M_{IJ}^m h^{-1} \exp[\iota \Delta_{IJ} kh] \\ &\approx \sum_{J \in \mathcal{S}_{JI}} M_{IJ}^m h^{-1} \bigg[1 + \iota \Delta_{IJ} kh - \frac{1}{2!}\Delta_{IJ}^2 (kh)^2 + \cdots \bigg]. \end{aligned} \tag{29}$$

By using the symmetry property of the mass and stiffness matrices, the summations of the terms with odd orders of (kh) in Eqs. (28) and (29) vanish. At the same time, the linear completeness condition of meshfree approximation immediately gives $\sum_{J \in \mathcal{S}_{JI}} K_{IJ} h = 0$. Thus Eqs. (28) and (29) can be recast as:

$$\vartheta \approx -\frac{1}{2!} \sum_{J \in \mathcal{S}_{JI}} K_{IJ} h \Delta_{IJ}^2 + \frac{1}{4!} \sum_{J \in \mathcal{S}_{JI}} K_{IJ} h \Delta_{IJ}^4 (kh)^2 + \cdots, \tag{30}$$

$$\ell \approx \sum_{J \in \mathcal{S}_{JI}} M_{IJ}^m h^{-1} - \frac{1}{2!} \sum_{J \in \mathcal{S}_{JI}} M_{IJ}^m h^{-1} \Delta_{IJ}^2 (kh)^2 + \cdots. \tag{31}$$

Consequently, according to Eq. (27), the frequency error for the proposed meshfree higher order mass matrix formulation becomes:

$$e_f = \frac{\omega^h}{\omega} - 1 \approx \frac{1}{2\vartheta}[-E_0 + E_2 (kh)^2 - E_4 (kh)^4], \tag{32}$$

where E_0, E_2 and E_4 are given by:

$$E_0 = \sum_{J \in \mathcal{S}_{JI}} M_{IJ}^m h^{-1} + \frac{1}{2!} \sum_{J \in \mathcal{S}_{JI}} K_{IJ} h \Delta_{IJ}^2, \tag{33}$$

$$E_2 = \frac{1}{2!} \sum_{J \in \mathcal{S}_{JI}} M_{IJ}^m h^{-1} \Delta_{IJ}^2 + \frac{1}{4!} \sum_{J \in \mathcal{S}_{JI}} K_{IJ} h \Delta_{IJ}^4, \tag{34}$$

$$E_4 = \frac{1}{4!} \sum_{J \in \mathcal{S}_{JI}} M_{IJ}^m h^{-1} \Delta_{IJ}^4 + \frac{1}{6!} \sum_{J \in \mathcal{S}_{JI}} K_{IJ} h \Delta_{IJ}^6. \tag{35}$$

Next, we shall prove in general that E_0 vanishes and the proposed mixed mass matrix provides a second-order accurate meshfree algorithm for frequency computation, and thus as special cases of the mixed mass matrix, both consistent and lumped mass matrices yield the second-order frequency accuracy. Furthermore, a superconvergent higher order mass matrix meshfree formulation with a fourth order accuracy can be established through selecting an optimal mass combination parameter.

Without loss of generality, it can be shown that the linearly complete meshfree shape functions with a uniform discretization have the following properties:

$$\int_\Omega \Psi_I(x) dx = h, \tag{36}$$

$$\int_\Omega \Psi_{I,x}(x) \sum_{J \in \mathcal{G}_J} \Psi_{J,x}(x)(x_J - x_I)^2 dx = -2h. \tag{37}$$

The theoretical proof of these properties is detailed in Appendix A. According to Eqs. (36) and (37), we have:

$$\frac{1}{2!} \sum_{J \in \mathcal{S}_{JI}} K_{IJ} h \Delta_{IJ}^2 = \frac{1}{2h} \int_\Omega \Psi_{I,x}(x) \sum_{J \in \mathcal{G}_J} \Psi_{J,x}(x)(x_J - x_I)^2 dx = -1, \tag{38}$$

$$\begin{aligned} \sum_{J \in \mathcal{S}_{JI}} M_{IJ}^m h^{-1} &= \frac{1}{h}(1-\gamma) \int_\Omega \Psi_I(x) dx + \frac{1}{h} \gamma \int_\Omega \Psi_I(x) \underbrace{\sum_{J \in \mathcal{G}_J} \Psi_J(x)}_{1} \, dx \\ &= \frac{1}{h} \int_\Omega \Psi_I(x) dx = 1. \end{aligned} \tag{39}$$

Consequently, the term E_0 in Eq. (32) becomes:

$$E_0 = \sum_{J \in \mathcal{S}_{JI}} M_{IJ}^m h^{-1} + \frac{1}{2!} \sum_{J \in \mathcal{S}_{JI}} K_{IJ} h \Delta_{IJ}^2 = 1 - 1 = 0. \tag{40}$$

Furthermore, with the aid of Eqs. (15) and (21), an expansion of E_2 given by Eq. (34) produces:

$$\begin{aligned} E_2 &= \frac{1}{2!}\sum_{J\in\mathcal{S}_{JI}} M_{IJ}^m h^{-1}\Delta_{IJ}^2 + \frac{1}{4!}\sum_{J\in\mathcal{S}_{JI}} K_{IJ}h\Delta_{IJ}^4 \\ &= \frac{1}{2!}\sum_{J\in\mathcal{S}_{JI}} [(1-\gamma)M_{IJ}^l + \gamma M_{IJ}]h^{-1}\Delta_{IJ}^2 + \frac{1}{4!}\sum_{J\in\mathcal{S}_{JI}} K_{IJ}h\Delta_{IJ}^4 \\ &= (1-\gamma)\sum_{J\in\mathcal{S}_{JI}}\sum_{K\in\mathcal{S}_{KI}} M_{IK}h^{-1}\underbrace{\delta_{IJ}\Delta_{IJ}^2}_{0} + \gamma\frac{1}{2!}\sum_{J\in\mathcal{S}_{JI}} M_{IJ}h^{-1}\Delta_{IJ}^2 \\ &\quad + \frac{1}{4!}\sum_{J\in\mathcal{S}_{JI}} K_{IJ}h\Delta_{IJ}^4. \end{aligned} \tag{41}$$

Therefore, imposing the condition of $E_2 = 0$ in Eq. (41) gives an optimal value of γ, denoted by γ_{opt}:

$$\gamma_{\text{opt}} = -\frac{\sum_{J\in\mathcal{S}_{JI}} K_{IJ}h\Delta_{IJ}^4}{12\sum_{J\in\mathcal{S}_{JI}} M_{IJ}h^{-1}\Delta_{IJ}^2}. \tag{42}$$

By virtue of Eq. (38), the term ϑ in Eq. (28) tends to be 1 when $h \to 0$, which also states that the denominator 2ϑ in Eq. (32) becomes a constant of 2 as $h \to 0$. Meanwhile, Eq. (26) says that Δ_{IJ} does not depend on h, and as a fact the terms $(M_{IJ}^m h^{-1})$ and $(K_{IJ}h)$ are not functions of h as well. As a result, the coefficients of $(kh)^2$ and $(kh)^4$ approach to constants as $h \to 0$. Therefore, the identity of Eq. (40) implies that we at least have a second-order accurate method regardless of the choice of the mass combination parameter γ, where $\gamma = 1$ and $\gamma = 0$ correspond to the consistent and lumped mass matrix formulations.

Further substituting the optimal mass combination parameter γ_{opt} back into the mixed mass matrix of Eq. (21) leads to the desired higher order mass matrix $\mathbf{M}^h$ with the following component:

$$M_{IJ}^h = M_{IJ}^m(\gamma_{\text{opt}}) = (1-\gamma_{\text{opt}})M_{IJ}^l + \gamma_{\text{opt}}M_{IJ}. \tag{43}$$

Now according to Eqs. (32), (40) and (42), the proposed higher order mass matrix $\mathbf{M}^h$ gives a fourth-order accurate algorithm for frequency computation.

It is noticed that in 1D case, the meshfree shape functions with linear basis functions degenerate to the piecewise linear finite element shape functions when the normalized support size of the meshfree kernel function tends to be 1. Under this circumstance, the nonzero terms of the mass and stiffness matrices associated with generic node x_I are: $K_{I(I-1)} = K_{I(I+1)} = -1/h$, $K_{II} = 2/h$, $M_{I(I-1)} = M_{I(I+1)} = h/6$, $M_{II} = 4h/6$, plugging these terms into Eq. (42) immediately yields $\gamma_{\text{opt}} = 1/2$, which is the classical result for the higher order mass matrix for linear finite elements.[1,32,33]

3.2. *2D meshfree higher order mass formulation*

In this sub-section, we present the 2D meshfree higher order mass matrix formulation which is still based upon the mixed mass matrix $\mathbf{M}^m$ defined by Eq. (21). While, in 2D case, the discrete harmonic wave associated with a control point $\mathbf{x}_J$ takes the following form:

$$\begin{cases} d_J(\mathbf{x},t) = d_0 \exp[\iota(k_x x_J + k_y y_J - \omega^h t)] \\ \ddot{d}_J(\mathbf{x},t) = -(\omega^h)^2 d_J(\mathbf{x},t) \end{cases}, \tag{44}$$

where k_x and k_y stand for the wave numbers in x and y directions, which can also be conveniently expressed by a single wave number k and the wave propagation angle θ as shown in Fig. 3:

$$k_x = k\cos\theta, \quad k_y = k\sin\theta. \tag{45}$$

Similar to the 1D formulation, substituting Eq. (44) into the discrete equation of motion given by Eq. (22) yields:

$$-(\omega^h)^2 \sum_{J\in\mathcal{S}_{JI}} M^m_{IJ} d_J + c^2 \sum_{J\in\mathcal{S}_{JI}} K_{IJ} d_J = 0. \tag{46}$$

Consequently, the discrete frequency ω^h can be expressed as:

$$\frac{\omega^h}{\omega} = \sqrt{\frac{(kh)^{-2}\sum_{J\in\mathcal{S}_{JI}} K_{IJ} d_J}{\sum_{J\in\mathcal{S}_{JI}} M_{IJ} h^{-2} d_J}} = \sqrt{\frac{(kh)^{-2}\sum_{J\in\mathcal{S}_{JI}} K_{IJ} \exp[\iota(k_x x_J + k_y y_J)]}{\sum_{J\in\mathcal{S}_{JI}} M_{IJ} h^{-2} \exp[\iota(k_x x_J + k_y y_J)]}}$$

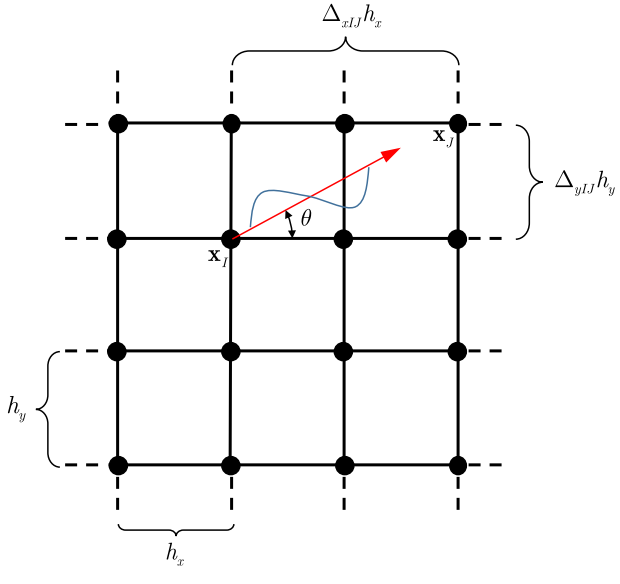

Fig. 3. Schematic illustration of 2D meshfree discretization and wave propagation angle.

$$= \sqrt{\frac{(kh)^{-2}\sum_{J\in\mathcal{S}_{JI}} K_{IJ}\exp[\iota(k_x x_J - k_x x_I + k_y y_J - k_y y_I)]}{\sum_{J\in\mathcal{S}_{JI}} M_{IJ}h^{-2}\exp[\iota(k_x x_J - k_x x_I + k_y y_J - k_y y_I)]}}$$
$$= \sqrt{\frac{(kh)^{-2}\sum_{J\in\mathcal{S}_{JI}} K_{IJ}\exp[\iota(\Delta_{xIJ}\cos\theta + \alpha\Delta_{yIJ}\sin\theta)kh]}{\sum_{J\in\mathcal{S}_{JI}} M_{IJ}h^{-2}\exp[\iota(\Delta_{xIJ}\cos\theta + \alpha\Delta_{yIJ}\sin\theta)kh]}}, \tag{47}$$

where $h_x = h, h_y = \alpha h, \alpha$ is the aspect ratio, h_x and h_y are the lengths between neighboring meshfree nodes in x and y directions, respectively. Δ_{xIJ} and Δ_{yIJ} are given by

$$\Delta_{xIJ} = \frac{x_J - x_I}{h_x}, \quad \Delta_{yIJ} = \frac{y_J - y_I}{h_y}. \tag{48}$$

Subsequently by invoking the Taylor's expansion,[39] Eq. (47) can also be recast into the formula given by Eq. (27), in which the corresponding parameters ϑ and ℓ are:

$$\begin{aligned}\vartheta &= (kh)^{-2}\sum_{J\in\mathcal{S}_{JI}} K_{IJ}\exp[\iota(\Delta_{xIJ}\cos\theta + \alpha\Delta_{yIJ}\sin\theta)kh] \\ &\approx -\frac{1}{2!}\sum_{J\in\mathcal{S}_{JI}} K_{IJ}(\Delta_{xIJ}\cos\theta + \alpha\Delta_{yIJ}\sin\theta)^2 \\ &\quad + \frac{1}{4!}\sum_{J\in\mathcal{S}_{JI}} K_{IJ}(\Delta_{xIJ}\cos\theta + \alpha\Delta_{yIJ}\sin\theta)^4(kh)^2 + \cdots \\ &= -\frac{1}{2!}\sum_{J\in\mathcal{S}_{JI}} K_{IJ}\tilde{\Delta}_{IJ}^{\,2} + \frac{1}{4!}\sum_{J\in\mathcal{S}_{JI}} K_{IJ}\tilde{\Delta}_{IJ}^{\,4}(kh)^2 + \cdots,\end{aligned} \tag{49}$$

$$\begin{aligned}\ell &= \sum_{J\in\mathcal{S}_{JI}} M_{IJ}^m h^{-2}\exp[\iota(\Delta_{xIJ}\cos\theta + \alpha\Delta_{yIJ}\sin\theta)kh] \\ &\approx \sum_{J\in\mathcal{S}_{JI}} M_{IJ}^m h^{-2} - \frac{1}{2!}\sum_{J\in\mathcal{S}_{JI}} M_{IJ}h^{-2}(\Delta_{xIJ}\cos\theta + \alpha\Delta_{yIJ}\sin\theta)^2(kh)^2 + \cdots \\ &= \sum_{J\in\mathcal{S}_{JI}} M_{IJ}^m h^{-1} - \frac{1}{2!}\sum_{J\in\mathcal{S}_{JI}} M_{IJ}^m h^{-1}\tilde{\Delta}_{IJ}^{\,2}(kh)^2 + \cdots,\end{aligned} \tag{50}$$

where for convenience of expression, we introduce the following notation $\tilde{\Delta}_{IJ}$ which is independent of the generic nodal distance h:

$$\tilde{\Delta}_{IJ} = \Delta_{xIJ}\cos\theta + \alpha\Delta_{yIJ}\sin\theta. \tag{51}$$

It is noted that with the above notation of $\tilde{\Delta}_{IJ}$, the terms ϑ and ℓ exhibit identical forms for both 1D and 2D cases, as shown in Eqs. (30), (31), (49) and (50).

In accordance with Eq. (27), plugging Eqs. (49)–(51) into Eq. (47) leads to the frequency error for the 2D meshfree higher order mass matrix formulation:

$$e_f = \frac{\omega^h}{\omega} - 1 \approx \frac{1}{2\vartheta}[-E_0 + E_2(kh)^2 - E_4(kh)^4], \tag{52}$$

where E_0, E_2 and E_4 under this circumstance are given by:

$$E_0 = \sum_{J\in\mathcal{S}_{JI}} M^m_{IJ} h^{-2} + \frac{1}{2!}\sum_{J\in\mathcal{S}_{JI}} K_{IJ}\tilde{\Delta}^{\,2}_{IJ}, \tag{53}$$

$$E_2 = \frac{1}{2!}\sum_{J\in\mathcal{S}_{JI}} M^m_{IJ} h^{-2}\tilde{\Delta}^{\,2}_{IJ} + \frac{1}{4!}\sum_{J\in\mathcal{S}_{JI}} K_{IJ}\tilde{\Delta}^{\,4}_{IJ}, \tag{54}$$

$$E_4 = \frac{1}{4!}\sum_{J\in\mathcal{S}_{JI}} M^m_{IJ} h^{-1}\tilde{\Delta}^{\,4}_{IJ} + \frac{1}{6!}\sum_{J\in\mathcal{S}_{JI}} K_{IJ} h\tilde{\Delta}^{\,6}_{IJ}. \tag{55}$$

In the meantime, as shown in Appendix B, the following identities hold for 2D uniform meshfree discretization:

$$\int_\Omega \Psi_I(\mathbf{x}) d\Omega = h_x h_y, \tag{56}$$

$$\int_\Omega \nabla\Psi_I(\mathbf{x}) \cdot \sum_{J\in\mathcal{G}_J} \nabla\Psi_J(\mathbf{x})[(x_J - x_I)\cos\theta + (y_J - y_I)\sin\theta]^2 d\Omega = -2h_x h_y. \tag{57}$$

Accordingly, the first terms of ϑ and ℓ in Eqs. (49) and (50) become:

$$\begin{aligned}\frac{1}{2!}\sum_{J\in\mathcal{S}_{JI}} K_{IJ}\tilde{\Delta}^{\,2}_{IJ} &= \frac{1}{2h^2}\int_\Omega \nabla\Psi_I(\mathbf{x}) \cdot \sum_{J\in\mathcal{G}_J} \nabla\Psi_J(\mathbf{x})[(x_J - x_I)\cos\theta + (y_J - y_I)\sin\theta]^2 d\Omega \\ &= -\alpha, \end{aligned} \tag{58}$$

$$\sum_{J\in\mathcal{S}_{JI}} M^m_{IJ} h^{-2} = \frac{1}{h^2}\int_\Omega \Psi_I(\mathbf{x}) d\Omega = \alpha. \tag{59}$$

Thus, based on the definitions of mixed mass and stiffness matrices and with the aid of Eqs. (58) and (59), the parameter E_0 of Eq. (53) reduces to:

$$E_0 = \sum_{J\in\mathcal{S}_{JI}} M^m_{IJ} h^{-2} + \frac{1}{2!}\sum_{J\in\mathcal{S}_{JI}} K_{IJ}\tilde{\Delta}^{\,2}_{IJ} = \alpha - \alpha = 0. \tag{60}$$

A further step of letting $E_2 = 0$ in Eq. (54) leads to:

$$\begin{aligned} E_2 &= (1-\gamma)\frac{1}{2!}\sum_{J\in\mathcal{S}_{JI}} M^l_{IJ} h^{-2}\tilde{\Delta}^{\,2}_{IJ} + \gamma\frac{1}{2!}\sum_{J\in\mathcal{S}_{JI}} M_{IJ} h^{-2}\tilde{\Delta}^{\,2}_{IJ} + \frac{1}{4!}\sum_{J\in\mathcal{S}_{JI}} K_{IJ}\tilde{\Delta}^{\,4}_{IJ} \\ &= (1-\gamma)\frac{1}{2!}\sum_{J\in\mathcal{S}_{JI}}\sum_{K\in\mathcal{S}_{KI}} M_{IK} h^{-2}\underbrace{\delta_{IJ}\tilde{\Delta}^{\,2}_{IJ}}_{0} + \gamma\frac{1}{2!}\sum_{J\in\mathcal{S}_{JI}} M_{IJ} h^{-2}\tilde{\Delta}^{\,2}_{IJ} + \frac{1}{4!}\sum_{J\in\mathcal{S}_{JI}} K_{IJ}\tilde{\Delta}^{\,4}_{IJ} \\ &= \gamma\frac{1}{2!}\sum_{J\in\mathcal{S}_{JI}} M_{IJ} h^{-2}\tilde{\Delta}^{\,2}_{IJ} + \frac{1}{4!}\sum_{J\in\mathcal{S}_{JI}} K_{IJ}\tilde{\Delta}^{\,4}_{IJ} \\ &= 0. \end{aligned} \tag{61}$$

Equation (61) results in a 2D optimal mass combination parameter γ_{opt}:

$$\gamma_{\text{opt}} = -\frac{\sum_{J\in\mathcal{S}_{JI}} K_{IJ}\tilde{\Delta}_{IJ}^{4}}{12\sum_{J\in\mathcal{S}_{JI}} M_{IJ}^{CM}h^{-2}\tilde{\Delta}_{IJ}^{2}}. \tag{62}$$

An employment of γ_{opt} in the mixed mass matrix immediately gives the 2D meshfree higher order mass matrix $\mathbf{M}^h = \mathbf{M}^m(\gamma_{\text{opt}})$, which is described as well by Eq. (43).

Following exactly the same path as the previous discussion on frequency accuracy analysis for 1D formulation, in 2D case, the parameter ϑ in Eq. (52) tends to be the value of α as $h \to 0, \tilde{\Delta}_{IJ}$, $(M_{IJ}^m h^{-1})$ and $(K_{IJ}h)$ also do not depend on h. Thus the coefficients of various orders of (kh) tend to be constants as $h \to 0$. As a result,

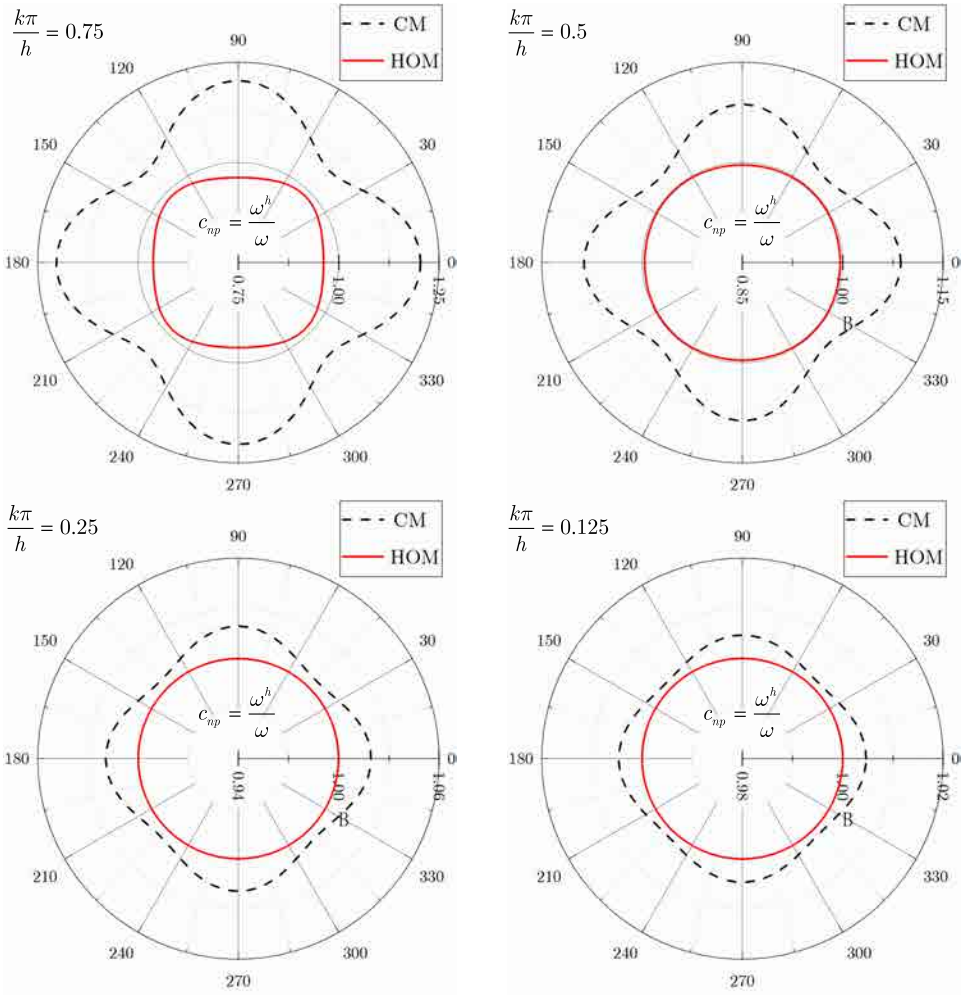

Eq. (52) confirms a second-order frequency accuracy for the conventional consistent and lumped mass matrices, and on the contrary, the proposed meshfree higher order mass matrix formulation is fourth-order accurate because of $E_0 = 0$ and $E_2 = 0$ under the condition of $\gamma = \gamma_{\text{opt}}$.

A close comparison of Eqs. (42) and (62) shows that 1D and 2D optimal mass combination parameters share a similar form. However, it is noted that in the 2D case, the discretization aspect ratio $\alpha = h_y/h_x$ and the wave propagation angle θ are embedded in $\tilde{\Delta}_{IJ}$ as shown in Eq. (51), thus γ_{opt} in Eq. (62) offers a feasible way to compute the frequencies associated with any wave propagation angle in a super-convergent manner. Figure 4 presents the dispersion properties of the consistent and higher order mass matrix formulations, in which a normalized support size of 1.3 is used and $c_{np} = \omega^h/\omega$ stands for the normalized phase speed. The dispersion results clearly demonstrate the superior accuracy of the meshfree higher order mass matrix formulation, compared with the standard consistent mass matrix approach.

4. Numerical Examples

4.1. *Vibration of 1D rod*

The free vibration of an elastic rod is first studied to assess the proposed meshfree higher order mass matrix formulation, in which three types of boundary conditions, namely, free-free, fixed-fixed and fixed-free boundary conditions, are considered. Without loss of generality, the geometry and material properties for the elastic rod are chosen as: length $L = 1$, cross-section area $A = 1$, material density $\rho = 1$ and Young's modulus $E = 1$. The analytical solutions for the elastic rod vibration problem with different kinds of boundary conditions are given by:

$$\omega_i = \begin{cases} ic\pi/L & \text{fixed-fixed rod} \\ (2i-1)c\pi/(2L) & \text{fixed-free rod} \\ (i-1)c\pi/L & \text{free-free rod} \end{cases}, \tag{63}$$

where $c = \sqrt{E/\rho}$.

In the meshfree vibration analysis, a linear basis function and a normalized support size of 1.3 for the kernel function are used to build the meshfree shape functions. The boundary conditions are enforced by the Lagrange multiplier method.[3] The frequency convergence is examined using 21, 41, 81 meshfree nodes and the corresponding results are presented in Figs. 5–7, in which CM, LM and HOM represent the consistent mass matrix formulation, the lumped mass matrix formulation and the higher order mass matrix formulation, respectively. The results of the first six frequencies for the elastic rod problem with fixed-fixed boundary condition are shown in Fig. 5, which obviously reveal that an expected superconvergence with a fourth-order accuracy is observed for the proposed meshfree HOM, whereas following the previous theoretical frequency error analysis, a second-order accuracy is attained by the standard CM and LM.

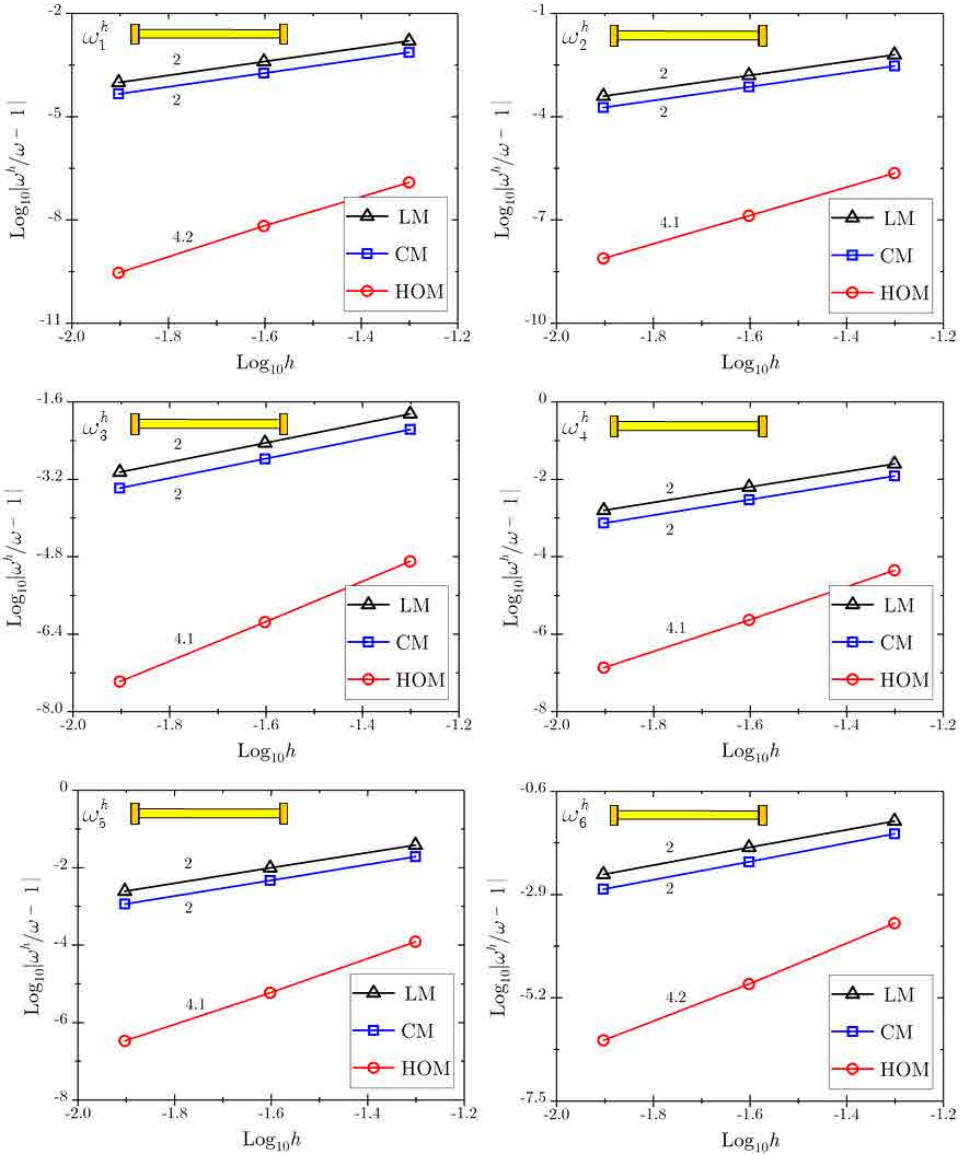

Fig. 5. Comparison of the first six frequencies for the elastic rod problem with fixed-fixed boundary condition.

Meanwhile, the frequency results corresponding to the fixed-free and free-free boundary conditions in Figs. 6 and 7 manifest a slight reduction of the theoretical superconvergence rate, say, from 4 to 3 for the proposed meshfree HOM, but in general much more favorable convergence rates and accuracy for different frequencies are still produced by the present method, in contrast to the standard CM and LM. The reason for this convergence rate reduction is that the practical meshfree shape

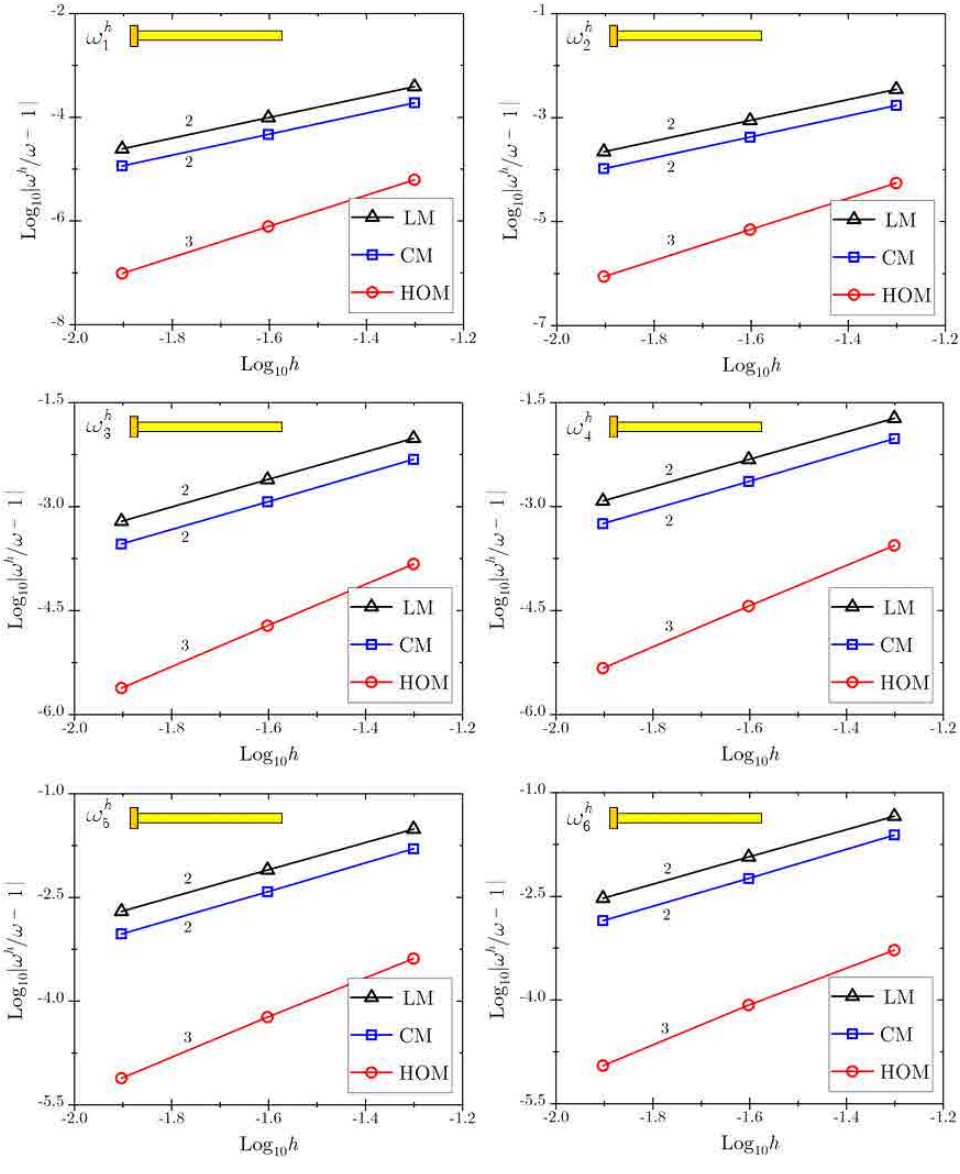

Fig. 6. Comparison of the first six frequencies for the elastic rod problem with fixed-free boundary condition.

functions are not uniform throughout the problem domain and exhibit the boundary truncation effect, which somehow deviates from the hypothesis in the previous theoretical development. This boundary effect is more pronounced in case of the free boundary condition, since for the fixed boundary condition, the corresponding degrees of freedom are constrained in the frequency computation. Furthermore, the

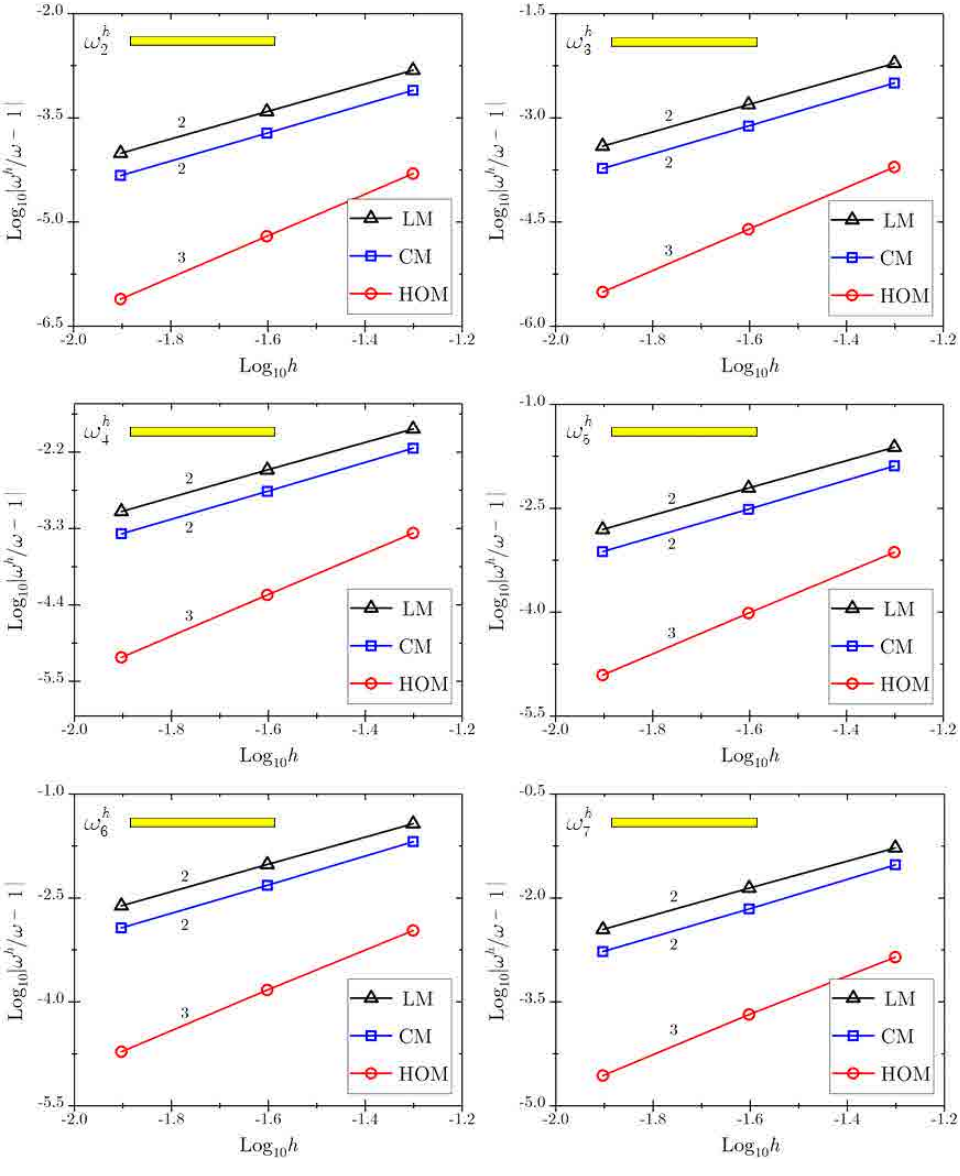

Fig. 7. Comparison of the first six frequencies for the elastic rod problem with free-free boundary condition.

nonuniform meshfree discretizations in Fig. 8 are employed to assess the proposed method. The corresponding results in Fig. 9 reveal that in the case of nonuniform discretizations, the convergence rates of the proposed HOM are slightly below the expected superconvergence rate for some frequencies; however, much better accuracy and higher convergence rates are attained as well by HOM compared with CM and

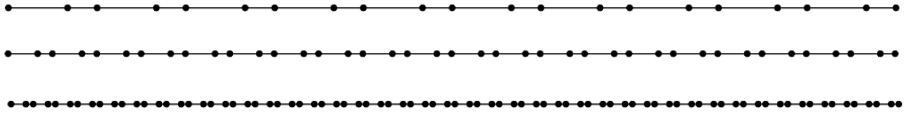

Fig. 8. Nonuniform meshfree discretizations for the elastic rod problem: 21 nodes, 41 nodes, 81 nodes.

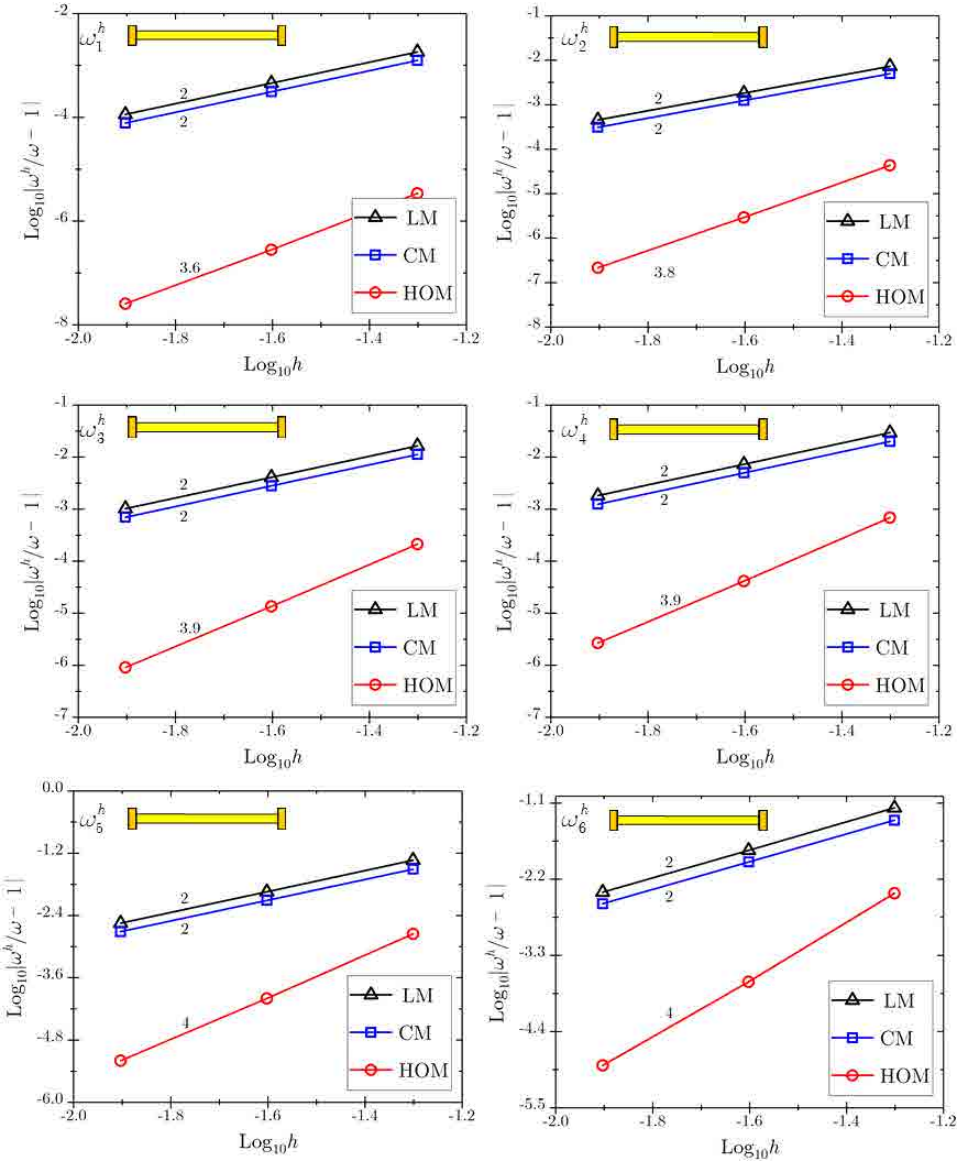

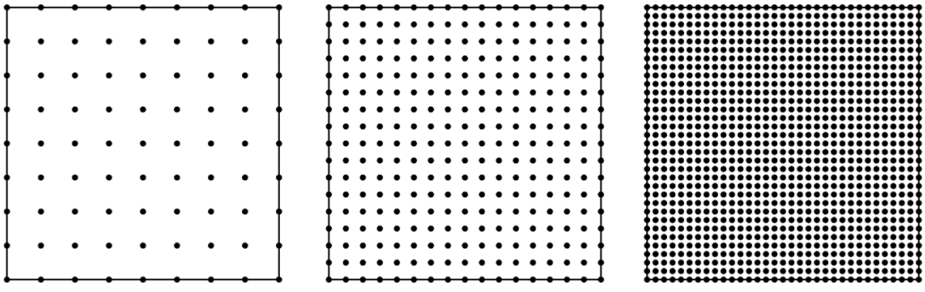

Fig. 10. Meshfree discretizations for the square membrane problem: 81 nodes, 289 nodes, 1,089 nodes.

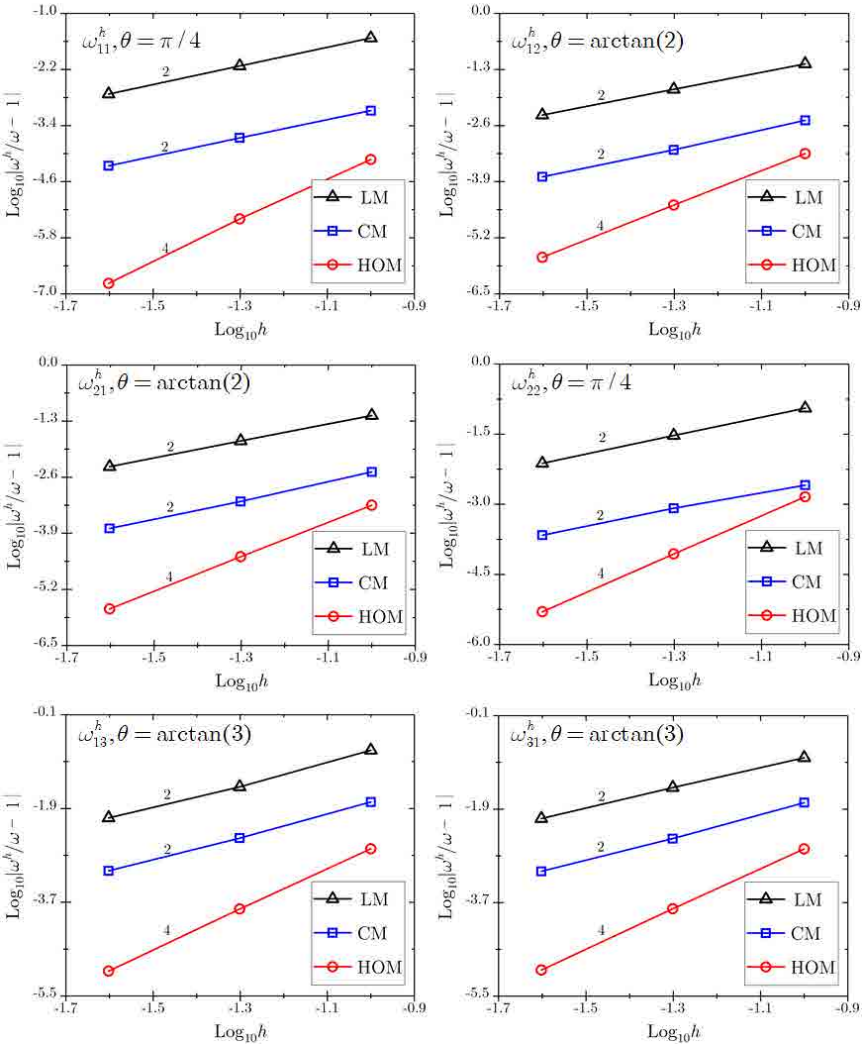

Fig. 11. Comparison of the first six frequencies for the square membrane problem.

LM. As a whole, the 1D results herein do demonstrate the superior performance of the present meshfree HOM.

4.2. *Vibration of square membrane*

A square membrane structure is considered here to testify the proposed 2D meshfree higher order mass matrix formulation. The membrane is subjected to the four-side fixed boundary condition. The analytical frequency for this problem is:

$$\omega_{ij} = \pi c \sqrt{\left(\frac{i}{L_x}\right)^2 + \left(\frac{j}{L_y}\right)^2}, \tag{64}$$

where $c = \sqrt{T/\rho}, T$ denotes the membrane tension and ρ represents the material density, L_x and L_y are the lengths of the membrane structure in x and y directions, respectively. Without loss of generality, the following parameters are employed in the frequency computation: $L_x = L_y = 1, T = 1$ and $\rho = 1$. The progressively refined meshfree discretizations with 81, 289 and 1,089 nodes for this problem are depicted in Fig. 10. The meshfree shape functions are formulated with the linear basis function and the cubic B-spline kernel function with a normalized support size of 1.4. The first six frequencies for the square membrane problem, namely, $\omega^h_{11}, \omega^h_{12}, \omega^h_{21}, \omega^h_{22}, \omega^h_{13}$ and ω^h_{31}, are plotted in Fig. 11, in which comparison is also given for the three methods, CM, LM and the proposed HOM. It is in clear evidence that the present meshfree HOM leads to fourth-order accurate frequencies, which outperforms the second-order accurate results by the conventional CM and LM.

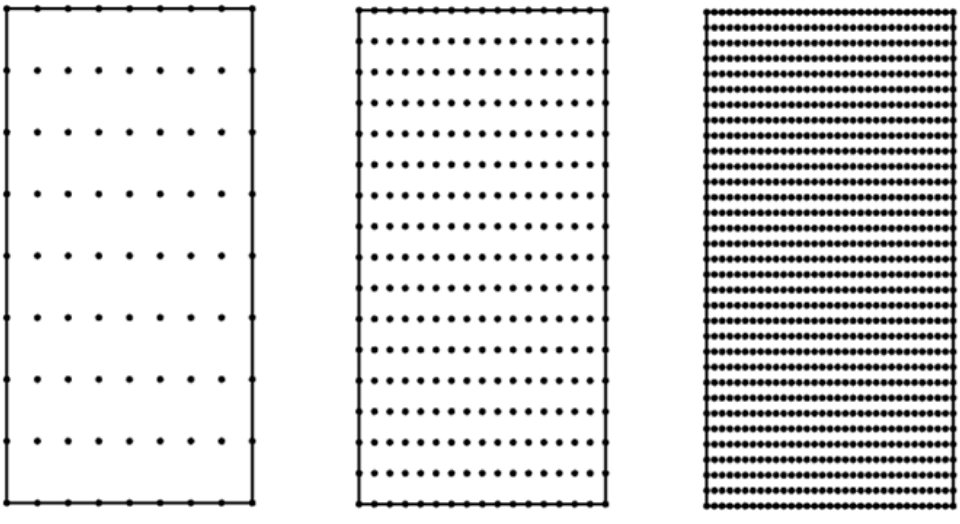

4.3. *Vibration of rectangular membrane*

The rectangular membrane problem with a four-side fixed boundary condition is further investigated to validate the proposed method of HOM. The rectangular membrane has the dimensions of $L_x = 1$ and $L_y = 2$. The analytical solution of this problem is also given by Eq. (64). Other material properties take unit values. Figure 12 lists the three meshfree discretizations for the rectangular membrane

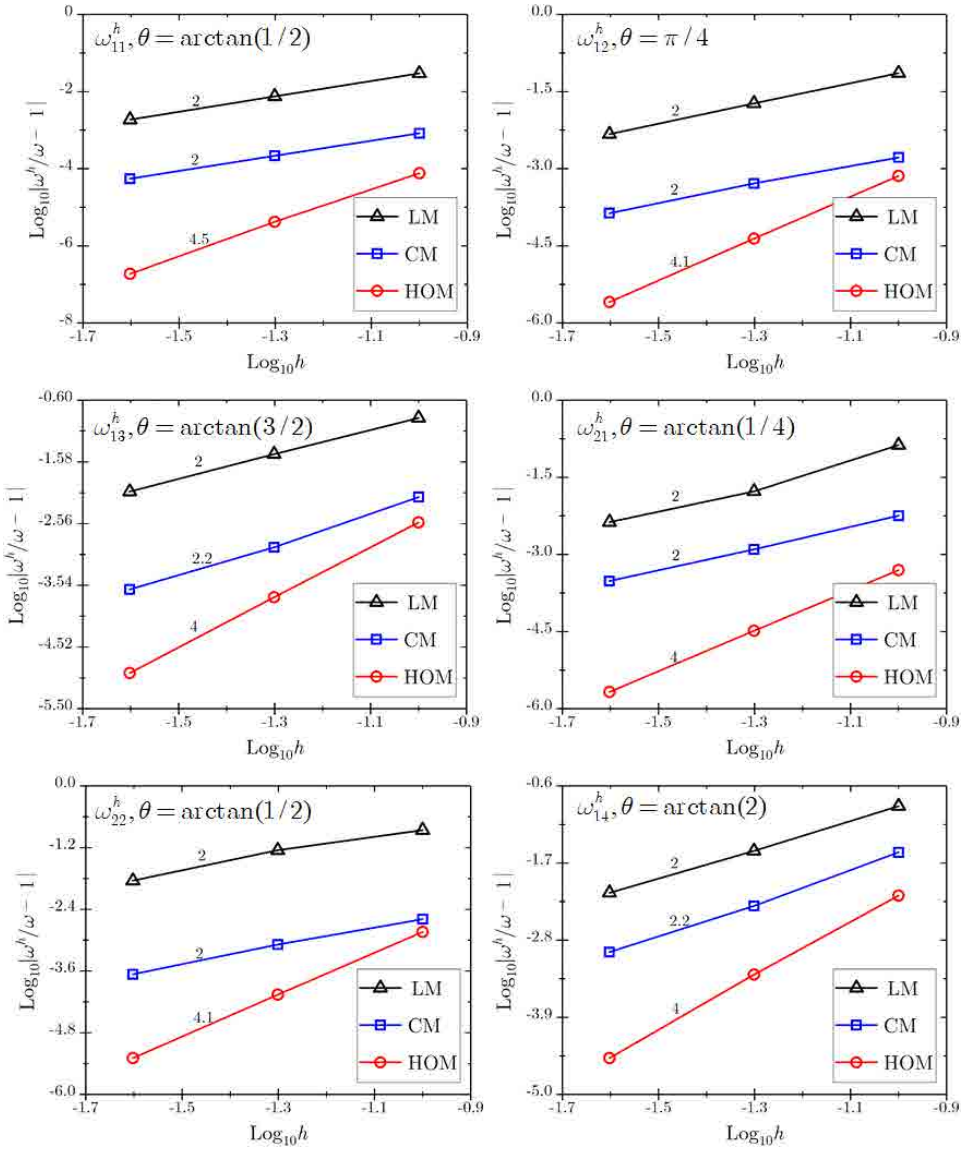

Fig. 13. Comparison of the first six frequencies for the rectangular membrane problem.

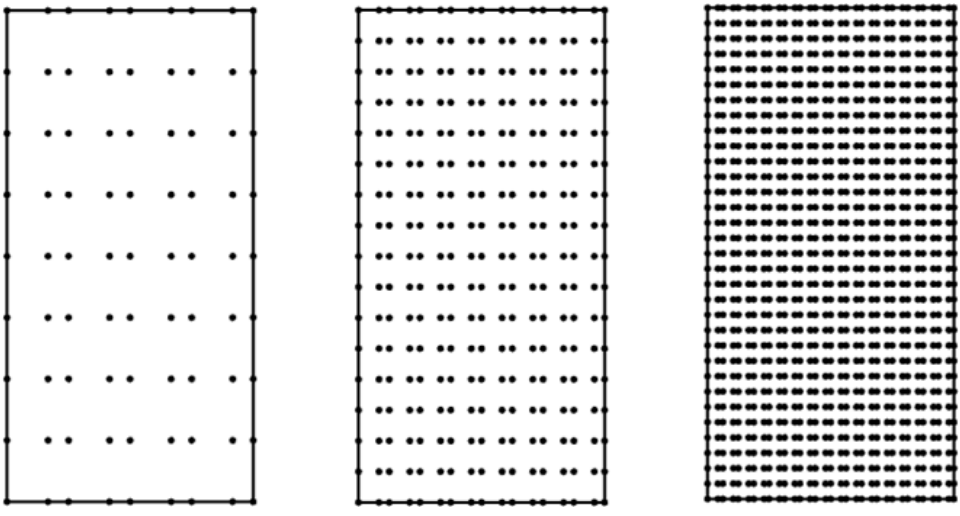

Fig. 14. Nonuniform meshfree discretizations for the rectangular membrane problem: 81 nodes, 289 nodes and 1,089 nodes.

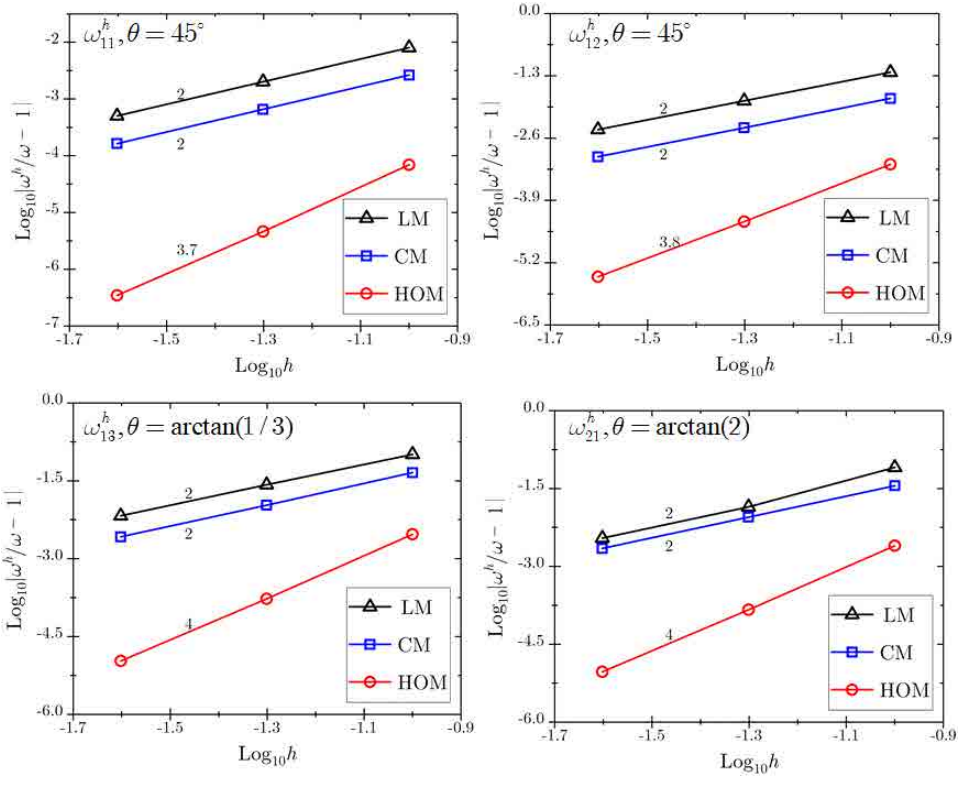

Fig. 15. Comparison of the first six frequencies for the rectangular membrane problem using nonuniform meshfree discretizations.

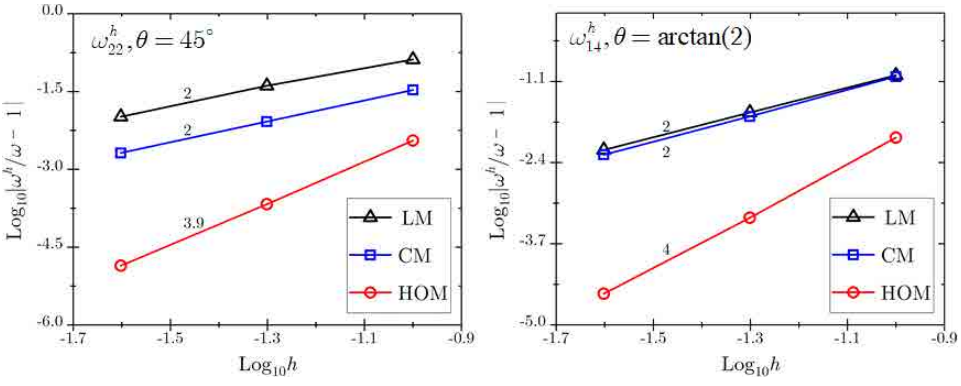

Fig. 15. (*Continued*)

problem, in which 81, 289 and 1,089 meshfree nodes are used. Similar to the previous square membrane problem, a linear basis function is adopted and the normalized support size of the cubic B-spline kernel function is set to be 1.4. The first six frequencies $\omega_{11}^h, \omega_{12}^h, \omega_{13}^h, \omega_{21}^h, \omega_{22}^h$ and ω_{14}^h computed by various methods, LM, CM and HOM, are illustrated in Fig. 13. These results once again confirmed the superconvergence of the proposed HOM with a fourth-order frequency accuracy, which compares favorably with the second accurate frequencies produced by CM and LM. Meanwhile, it can be seen that the proposed HOM enables a superconvergent meshfree computation of frequencies related to any wave propagation angle. In addition, the superior performance of the proposed HOM over CM and LM using the nonuniform discretizations in Fig. 14 is evidently displayed by the results in Fig. 15.

5. Conclusions

An accurate meshfree formulation was presented for structural vibration analysis. The proposed meshfree formulation was realized through the construction of higher order mass matrix. The present formulation is quite general and does not require explicit expressions or specific forms of the shape functions, which is actually important as the meshfree shape functions usually do not have explicit forms like the finite element shape functions. A frequency error measure containing general mass and stiffness matrix entries was deduced from the generic equation of motion. Subsequently, some interesting properties for meshfree mass and stiffness matrices were illustrated purely based on the consistency conditions, where there is no involvement of explicit mass or stiffness matrix expressions. Consequently, it was shown that the conventional consistent and lumped mass matrices give second-order accurate frequencies when the moving least squares or reproducing meshfree approximation with linear basis function is utilized. In contrast, an optimal combination of the consistent and lumped mass matrices does provide a superconvergent meshfree higher order mass matrix with an accuracy order of 4 for frequency computation. It was

demonstrated that both 1D and 2D optimal mass combination parameters have nearly identical forms. It is also noted that the discretization aspect ratio and the wave propagation angle are embedded into the 2D optimal mass combination parameter, which allows a superconvergent computation of frequencies associated with any wave propagation angle. Numerical results evidently revealed that the proposed meshfree higher order mass matrix formulation gives a superior performance regarding the convergence rate and accuracy of frequency analysis, compared with the standard meshfree formulations with consistent or lumped mass matrices.

Acknowledgment

The support of this work by the National Natural Science Foundation of China (11772280, 11472233) is gratefully acknowledged.

Appendix A.

In Appendix A, we detail the proof of Eqs. (36) and (37). Without loss of generality, we consider the uniform discretization as shown in Fig. A.1, in which x_Is denote the meshfree nodes. Due to the symmetry and periodicity of meshfree shape functions as depicted in Fig. A.1, the following relationships for meshfree shape functions and their derivatives are evident:

$$\Psi_I(x) = \Psi_J(x + x_J - x_I), \tag{A.1}$$

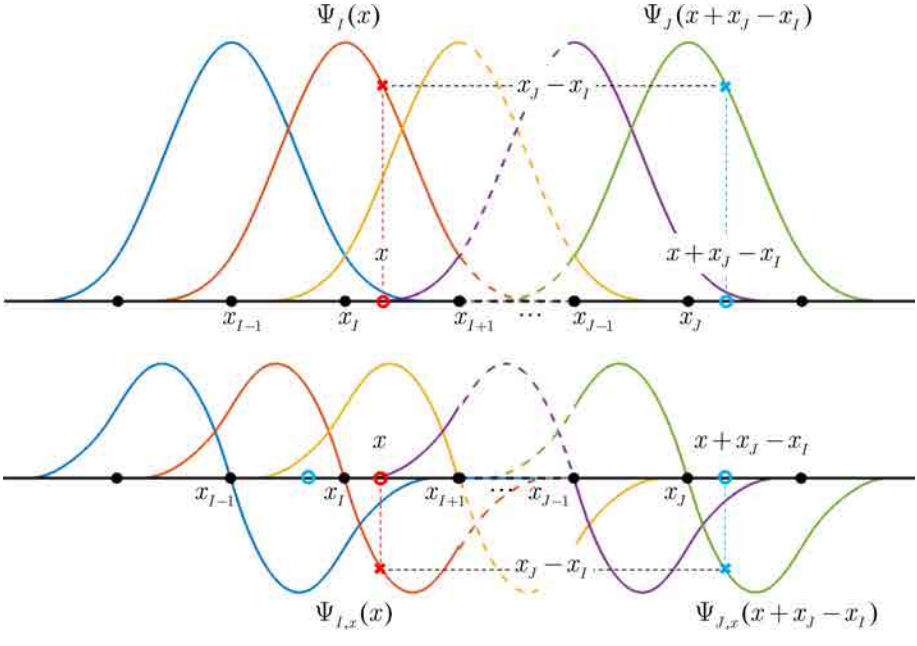

Fig. A.1. 1D uniform meshfree discretization: Shape functions and their derivatives.

$$\Psi_{I,x}(x) = \Psi_{J,x}(x + x_J - x_I). \tag{A.2}$$

We also recall the following consistency conditions for meshfree shape functions according to Eq. (5):

$$\sum_{I\in\mathcal{G}_I} \Psi_I(x) = 1, \quad \sum_{I\in\mathcal{G}_I} \Psi_{I,x}(x) = 0, \tag{A.3}$$

$$\sum_{I\in\mathcal{G}_I} \Psi_{I,x}(x)(x_I - x) = 1, \quad \sum_{I\in\mathcal{G}_I} \Psi_{I,x}(x)(x - x_I) = -1. \tag{A.4}$$

By using Eq. (A.1), Eq. (36) can be recast as:

$$\begin{aligned}
\int_\Omega \Psi_I(x)dx &= \sum_{N\in\mathcal{S}_{(I+N)I}} \int_{x_{I-N}}^{x_{I-N+1}} \Psi_I(x)dx \\
&= \sum_{N\in\mathcal{S}_{(I+N)I}} \int_{x_{I-N}}^{x_{I-N+1}} \Psi_{I+N}(x + x_{I+N} - x_I)dx \\
&= \sum_{N\in\mathcal{S}_{(I+N)I}} \int_{x_{I-N}+x_{I+N}-x_I}^{x_{I-N+1}+x_{I+N}-x_I} \Psi_{I+N}(x)dx \\
&= \sum_{N\in\mathcal{S}_{(I+N)I}} \int_{x_I}^{x_{I+1}} \Psi_{I+N}(x)dx \\
&= \int_{x_I}^{x_I+h} \underbrace{\sum_{(I+N)\in\mathcal{G}_{I+N}} \Psi_{I+N}(x)}_{1} \, d\Omega \\
&= h,
\end{aligned} \tag{A.5}$$

where the relationship of $x_{I-N} + x_{I+N} = 2x_I$ and the partition of unity property of meshfree shape functions are used.

As for Eq. (37), it can be divided into two parts:

$$\begin{aligned}
&\int_\Omega \Psi_{I,x}(x) \sum_{J\in\mathcal{G}_J} \Psi_{J,x}(x)(x_J - x_I)^2 dx \\
&\quad = \int_\Omega \Psi_{I,x}(x) \sum_{J\in\mathcal{G}_J} \Psi_{J,x}(x)(x_J - x_I)(x_J - x + x - x_I)dx \\
&\quad = \mathcal{T}_1 + \mathcal{T}_2
\end{aligned} \tag{A.6}$$

with

$$\begin{cases}
\mathcal{T}_1 = \displaystyle\int_\Omega \Psi_{I,x}(x) \sum_{J\in\mathcal{G}_J} \Psi_{J,x}(x)(x_J - x_I)(x_J - x)dx \\
\mathcal{T}_2 = \displaystyle\int_\Omega \Psi_{I,x}(x) \sum_{J\in\mathcal{G}_J} \Psi_{J,x}(x)(x_J - x_I)(x - x_I)dx
\end{cases}. \tag{A.7}$$

According to Eq. (A.2) and the consistency conditions for the derivatives of meshfree shape functions as described in Eqs. (A.3) and (A.4), the two parts $\mathcal{T}_1$ and $\mathcal{T}_2$ in Eq. (A.6) turn out to be:

$$
\begin{aligned}
\mathcal{T}_1 &= \int_\Omega \Psi_{I,x}(x) \sum_{J\in\mathcal{G}_J} \Psi_{J,x}(x)(x_J - x_I)(x_J - x)dx \\
&= \sum_{N\in\mathcal{S}_{(I+N)I}} \int_{x_{I-N}}^{x_{I-N+1}} \Psi_{I,x}(x) \sum_{M\in\mathcal{S}_{(I-N+M)I}} \Psi_{I-N+M,x}(x)(x_{I-N+M} - x_I)(x_{I-N+M} - x)dx \\
&= \sum_{N\in\mathcal{S}_{(I+N)I}} \int_{x_{I-N}}^{x_{I-N+1}} \sum_{M\in\mathcal{S}_{(I+M)(I+N)}} \left\{ \begin{array}{c} \Psi_{I+N,x}(x + x_{I+N} - x_I)\Psi_{I+M,x}(x + x_{I+N} - x_I) \\ \times\ (x_{I+M} - x_{I+N})(x_{I-N+M} - x) \end{array} \right\} dx \\
&= \sum_{N\in\mathcal{S}_{(I+N)I}} \int_{x_{I-N}+x_{I+N}-x_I}^{x_{I-N+1}+x_{I+N}-x_I} \sum_{M\in\mathcal{S}_{(I+M)(I+N)}} \left\{ \begin{array}{c} \Psi_{I+N,x}(x)\Psi_{I+M,x}(x)(x_{I+M} - x_{I+N}) \\ \times\ (x_{I-N+M} - x + x_{I+N} - x_I) \end{array} \right\} dx \\
&= \sum_{N\in\mathcal{S}_{(I+N)I}} \int_{x_I}^{x_I+h} \Psi_{I+N,x}(x) \sum_{M\in\mathcal{S}_{(I+M)(I+N)}} \Psi_{I+M,x}(x)(x_{I+M} - x_{I+N})(x_{I+M} - x)dx \\
&= \int_{x_I}^{x_I+h} \sum_{M\in\mathcal{S}_{(I+M)(I+N)}} \underbrace{\sum_{(I+N)\in\mathcal{G}_{I+N}} \Psi_{I+N,x}(x)(x_{I+M} - x_{I+N})}_{-1}\ \Psi_{I+M,x}(x)(x_{I+M} - x)dx \\
&= -\int_{x_I}^{x_I+h} \underbrace{\sum_{(I+M)\in\mathcal{G}_{I+M}} \Psi_{I+M,x}(x)(x_{I+M} - x)}_{1}\, dx = -h,
\end{aligned}
\tag{A.8}
$$

$$
\begin{aligned}
\mathcal{T}_2 &= \int_\Omega \Psi_{I,x}(x) \underbrace{\sum_{J\in\mathcal{G}_J} \Psi_{J,x}(x)(x_J - x_I)}_{1} (x - x_I)dx \\
&= \sum_{N\in\mathcal{S}_{(I+N)I}} \int_{x_{I-N}}^{x_{I-N+1}} \Psi_{I,x}(x)(x - x_I)dx \\
&= \sum_{N\in\mathcal{S}_{(I+N)I}} \int_{x_{I-N}}^{x_{I-N+1}} \Psi_{I+N,x}(x + x_{I+N} - x_I)(x - x_I)dx \\
&= \sum_{N\in\mathcal{S}_{(I+N)I}} \int_{x_{I-N}+x_{I+N}-x_I}^{x_{I-N+1}+x_{I+N}-x_I} \Psi_{I+N,x}(x)(x - x_{I+N})dx \\
&= \int_{x_I}^{x_I+h} \underbrace{\sum_{(I+N)\in\mathcal{G}_{I+N}} \Psi_{I+N,x}(x)(x - x_{I+N})}_{-1}\, dx \\
&= -h.
\end{aligned}
\tag{A.9}
$$

Consequently, a combination of Eqs. (A.8) and (A.9) yields:

$$\int_{\Omega} \Psi_{I,x}(x) \sum_{J \in \mathcal{G}_J} \Psi_{J,x}(x)(x_J - x_I)^2 d\Omega = -2h. \tag{A.10}$$

Appendix B.

In Appendix B, Eqs. (56) and (57) for 2D meshfree formulation are proved. Similar to the previous 1D proof, we consider a uniform 2D meshfree discretization as shown in Fig. B.1. For convenience of development, we introduce a double-index subscript notation for the meshfree nodes as well as the meshfree shape functions:

$$I = (i, j), \quad \mathbf{x}_I = (x_i, y_j), \quad \Psi_I(\mathbf{x}) = \Psi_{(i,j)}(\mathbf{x}). \tag{B.1}$$

As shown in Fig. B.1, a generic domain $\Omega_{(i,j)}$ defined by neighboring meshfree nodes is denoted by $\Omega_{(i,j)} = [x_i, x_{i+1}] \otimes [y_i, y_{i+1}]$, where $\otimes$ is the dyadic product. The periodicity of the meshfree shape functions and their derivatives once again give the following identities:

$$\Psi_{(i,j)}(\mathbf{x}) = \Psi_{(p,q)}(x + x_p - x_i, y + y_q - y_j), \tag{B.2}$$

$$\nabla\Psi_{(i,j)}(\mathbf{x}) = \nabla\Psi_{(p,q)}(x + x_p - x_i, y + y_q - y_j). \tag{B.3}$$

Meanwhile, the consistency conditions of 2D meshfree shape functions are given from Eq. (5):

$$\sum_{I \in \mathcal{G}_I} \Psi_I(\mathbf{x}) = 1, \quad \sum_{I \in \mathcal{G}_I} \nabla\Psi_I(\mathbf{x}) = \mathbf{0}, \tag{B.4}$$

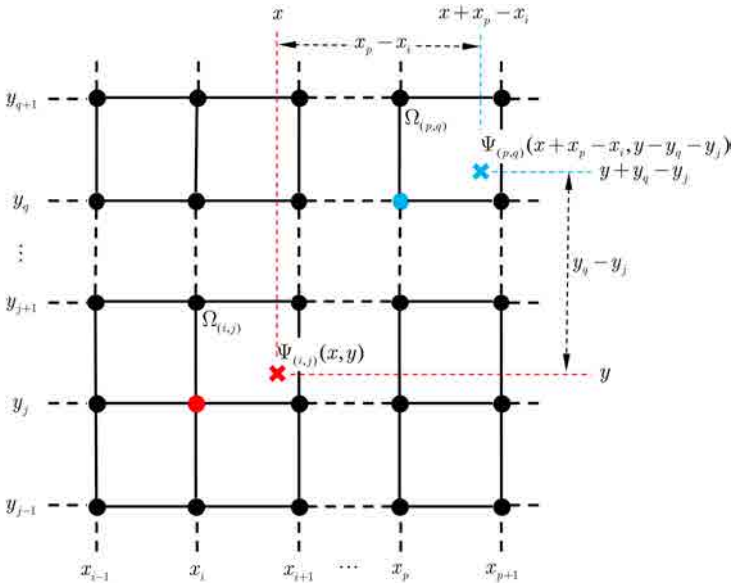

$$\begin{cases} \sum\limits_{I\in\mathcal{G}_I} \nabla\Psi_I(\mathbf{x})(x_I - x) = \begin{Bmatrix} 1 \\ 0 \end{Bmatrix}, \quad \sum\limits_{I\in\mathcal{G}_I} \nabla\Psi_I(\mathbf{x})(x - x_I) = -\begin{Bmatrix} 1 \\ 0 \end{Bmatrix} \\ \sum\limits_{I\in\mathcal{G}_I} \nabla\Psi_I(\mathbf{x})(y_I - y) = \begin{Bmatrix} 0 \\ 1 \end{Bmatrix}, \quad \sum\limits_{I\in\mathcal{G}_I} \nabla\Psi_I(\mathbf{x})(y - y_I) = -\begin{Bmatrix} 0 \\ 1 \end{Bmatrix} \end{cases}. \tag{B.5}$$

With the aid of Eq. (B.2), Eq. (56) can be proved as follows:

$$\begin{aligned} &\int_\Omega \Psi_I(\mathbf{x}) d\Omega \\ &\quad = \sum_{(m,n)\in\mathcal{S}_{(i+m,j+n)(i,j)}} \int_{\Omega_{(i-m,j-n)}} \Psi_{(i,j)}(\mathbf{x}) d\Omega \\ &\quad = \sum_{m,n\in\mathcal{S}_{(i+m,j+n)(i,j)}} \int_{\Omega_{(i-m,j-n)}} \Psi_{(i+m,j+n)}(x + x_{i+m} - x_i, y + y_{j+n} - y_j) d\Omega \\ &\quad = \int_{\Omega_{(i,j)}} \underbrace{\sum_{(i+m,j+n)\in\mathcal{G}_{(i+m,j+n)}} \Psi_{(i+m,j+n)}(\mathbf{x})}_{1} d\Omega \\ &\quad = A_{(i,j)} = h_x h_y, \end{aligned} \tag{B.6}$$

where it is noted that the two node number sets $\mathcal{G}_{(i+m,j+n)}$ and $\mathcal{S}_{(i+m,j+n)(i,j)}$ are defined as $\mathcal{G}_{(i+m,j+n)} = \{(i+m, j+n) | \mathbf{x} \in \text{supp}(x_{i+m}, y_{j+n})\}$ and $\mathcal{S}_{(i+m,j+n)(i,j)} = \{(m,n) | \mathcal{S}_{(i+m)(j+n)} \cap \mathcal{S}_{ij} \neq \emptyset\}$, respectively. $A_{(i,j)}$ represents the area of $\Omega_{(i,j)}$, and the following relationships are utilized in Eq. (B.6):

$$x_{i-m} + x_{i+m} = 2x_i, \quad y_{j-n} + x_{j+n} = 2x_j. \tag{B.7}$$

Equation (57) can be conveniently divided into three parts:

$$\int_\Omega \nabla\Psi_I(\mathbf{x}) \cdot \sum_{J\in\mathcal{G}_J} \nabla\Psi_J(\mathbf{x})[(x_J - x_I)\cos\theta + (y_J - y_I)\sin\theta]^2 d\Omega = \mathcal{H}_1 + \mathcal{H}_2 + \mathcal{H}_3 \tag{B.8}$$

with

$$\begin{cases} \mathcal{H}_1 = \int_\Omega \nabla\Psi_I(\mathbf{x}) \cdot \sum\limits_{J\in\mathcal{G}_J} \nabla\Psi_J(\mathbf{x})(x_J - x_I)^2 d\Omega \cos^2\theta \\ \mathcal{H}_2 = 2\int_\Omega \nabla\Psi_I(\mathbf{x}) \cdot \sum\limits_{J\in\mathcal{G}_J} \nabla\Psi_J(\mathbf{x})(x_J - x_I)(y_J - y_I) d\Omega \sin\theta\cos\theta \\ \mathcal{H}_3 = \int_\Omega \nabla\Psi_I(\mathbf{x}) \cdot \sum\limits_{J\in\mathcal{G}_J} \nabla\Psi_J(\mathbf{x})(y_J - y_I)^2 d\Omega \sin^2\theta \end{cases}. \tag{B.9}$$

The first part $\mathcal{H}_1$ in Eq. (B.8) can be subdivided into two terms, say $\mathcal{T}_1$ and $\mathcal{T}_2$, as follows:

$$\begin{aligned}\mathcal{H}_1 &= \int_\Omega \nabla\Psi_I(\mathbf{x}) \cdot \sum_{J\in\mathcal{G}_J} \nabla\Psi_J(\mathbf{x})(x_J - x_I)^2 d\Omega \cos^2\theta \\ &= \int_\Omega \nabla\Psi_I(\mathbf{x}) \cdot \sum_{J\in\mathcal{G}_J} \nabla\Psi_J(\mathbf{x})(x_J - x_I)[(x_J - x) + (x - x_I)] d\Omega \cos^2\theta \\ &= \mathcal{T}_1 + \mathcal{T}_2 \end{aligned} \tag{B.10}$$

with

$$\begin{cases} \mathcal{T}_1 = \displaystyle\int_\Omega \nabla\Psi_I(\mathbf{x}) \cdot \sum_{J\in\mathcal{G}_J} \nabla\Psi_J(\mathbf{x})(x_J - x_I)(x_J - x) d\Omega \cos^2\theta \\ \mathcal{T}_2 = \displaystyle\int_\Omega \nabla\Psi_I(\mathbf{x}) \cdot \sum_{J\in\mathcal{G}_J} \nabla\Psi_J(\mathbf{x})(x_J - x_I)(x - x_I) d\Omega \cos^2\theta \end{cases}. \tag{B.11}$$

Thereafter, based on the periodicity relationship of Eq. (B.3) and the consistency conditions for the derivatives of meshfree shape functions as indicated in Eqs. (B.4) and (B.5), we arrive at:

$$\begin{aligned}\mathcal{T}_1 &= \int_\Omega \nabla\Psi_I(\mathbf{x}) \cdot \sum_{J\in\mathcal{G}_J} \nabla\Psi_J(\mathbf{x})(x_J - x_I)(x_J - x) d\Omega \\ &= \sum_{(m,n)\in\mathcal{S}_{(i+m,j+n)(i,j)}} \int_{\Omega_{(i-m,j-n)}} \nabla\Psi_{(i,j)}(\mathbf{x}) \\ &\quad \cdot \sum_{(s,t)\in\mathcal{S}_{(i-m+s,j-n+t)(i,j)}} \left\{ \begin{array}{l} \nabla\Psi_{(i-m+s,j-n+t)}(\mathbf{x}) \\ \quad \times\ (x_{i-m+s} - x_i)(x_{i-m+s} - x) \end{array} \right\} d\Omega \\ &= \sum_{(m,n)\in\mathcal{S}_{(i+m,j+n)(i,j)}} \int_{\Omega_{(i-m,j-n)}} \sum_{(s,t)\in\mathcal{S}_{(i+s,j+t)(i+m,j+n)}} \\ &\quad \times \left\{ \begin{array}{l} \nabla\Psi_{(i+m,j+n)}(x + x_{i+m} - x_i, y + y_{j+n} - y_j) \\ \quad \cdot\ \nabla\Psi_{(i+s,j+t)}(x + x_{i+m} - x_i, y + y_{j+n} - y_j) \\ \quad \times\ (x_{i-m+s} - x_i)(x_{i-m+s} - x + x_{i+m} - x_i) \end{array} \right\} d\Omega \\ &= \int_{\Omega_{(i,j)}} \sum_{(s,t)\in\mathcal{S}_{(i+s,j+t)(i,j)}} \left\{ \begin{array}{l} \underbrace{\displaystyle\sum_{(i+m,j+n)\in\mathcal{G}_{(i+m,j+n)}} \nabla\Psi_{(i+m,j+n)}(\mathbf{x})(x_{i+s} - x_{i+m})}_{\{-1\ 0\}^T} \\ \quad \cdot\ \nabla\Psi_{(i+s,j+t)}(\mathbf{x})(x_{i+s} - x) \end{array} \right\} d\Omega \\ &= -\int_{\Omega_{(i,j)}} \underbrace{\sum_{(i+s,j+t)\in\mathcal{G}_{(i+s,j+t)}} \Psi_{(i+s,j+t),x}(\mathbf{x})(x_{i+s} - x)}_{1}\, d\Omega \\ &= -A_{(i,j)} = -h_x h_y, \end{aligned} \tag{B.12}$$

$$
\begin{aligned}
\mathcal{T}_2 &= \int_\Omega \nabla\Psi_I(\mathbf{x}) \cdot \underbrace{\sum_{J\in\mathcal{G}_J} \nabla\Psi_J(\mathbf{x})(x_J - x_I)}_{\{1\ 0\}^T} (x - x_I) d\Omega \\
&= \int_\Omega \Psi_{I,x}(\mathbf{x})(x - x_I) d\Omega \\
&= \sum_{(m,n)\in\mathcal{S}_{(i+m,j+n)(i,j)}} \int_{\Omega_{(i-m,j-n)}} \Psi_{(i+m,j+n),x} \\
&\quad \times (x + x_{i+m} - x_i, y + y_{j+n} - y_j)(x - x_i) d\Omega \\
&= \int_{\Omega_{(i,j)}} \underbrace{\sum_{(i+m,j+n)\in\mathcal{G}_{(i+m,j+n)}} \Psi_{(i+m,j+n),x}(\mathbf{x})(x - x_i)}_{-1} d\Omega \\
&= -A_{(i,j)} = -h_x h_y. \qquad \text{(B.13)}
\end{aligned}
$$

As a result, the first part $\mathcal{H}_1$ in Eq. (B.8) finally becomes:

$$
\mathcal{H}_1 = \int_\Omega \nabla\Psi_I(\mathbf{x}) \cdot \sum_{J\in\mathcal{G}_J} \nabla\Psi_J(\mathbf{x})(x_J - x_I)^2 d\Omega \cos^2\theta = -2h_x h_y \cos^2\theta. \qquad \text{(B.14)}
$$

Following a similar procedure as the derivation of $\mathcal{H}_1$, the third part $\mathcal{H}_3$ in Eq. (B.8) can be shown as:

$$
\mathcal{H}_3 = \int_\Omega \nabla\Psi_I(\mathbf{x}) \cdot \sum_{J\in\mathcal{G}_J} \nabla\Psi_J(\mathbf{x})(y_J - y_I)^2 d\Omega \sin^2\theta = -2h_x h_y \sin^2\theta. \qquad \text{(B.15)}
$$

Now the only left part in Eq. (B.8) is $\mathcal{H}_2$, which can be conveniently split into two parts:

$$
\begin{aligned}
\mathcal{H}_2 &= \int_\Omega \nabla\Psi_I(\mathbf{x}) \cdot \sum_{J\in\mathcal{G}_J} \nabla\Psi_J(\mathbf{x})(x_J - x_I)(y_J - y_I) d\Omega \\
&= \int_\Omega \nabla\Psi_I(\mathbf{x}) \cdot \sum_{J\in\mathcal{G}_J} \nabla\Psi_J(\mathbf{x})(x_J - x_I)(y_J - y + y - y_I) d\Omega \\
&= \mathcal{R}_1 + \mathcal{R}_2 \qquad \text{(B.16)}
\end{aligned}
$$

with

$$
\begin{cases}
\mathcal{R}_1 = \displaystyle\int_\Omega \nabla\Psi_I(\mathbf{x}) \cdot \sum_{J\in\mathcal{G}_J} \nabla\Psi_J(\mathbf{x})(x_J - x_I)(y_J - y) d\Omega \\
\mathcal{R}_2 = \displaystyle\int_\Omega \nabla\Psi_I(\mathbf{x}) \cdot \sum_{J\in\mathcal{G}_J} \nabla\Psi_J(\mathbf{x})(x_J - x_I)(y - y_I) d\Omega
\end{cases}. \qquad \text{(B.17)}
$$

It is straightforward to verify that both $\mathcal{R}_1$ and $\mathcal{R}_2$ identically vanish by using the consistency conditions:

$$\begin{aligned}
\mathcal{R}_1 &= \int_\Omega \nabla\Psi_I(\mathbf{x}) \cdot \sum_{J\in\mathcal{G}_J} \nabla\Psi_J(\mathbf{x})(x_J - x_I)(y_J - y)d\Omega \\
&= \sum_{(m,n)\in\mathcal{S}_{(i+m,j+n)(i,j)}} \int_{\Omega_{(i-m,j-n)}} \nabla\Psi_{(i,j)}(\mathbf{x}) \\
&\quad \cdot \sum_{(s,t)\in\mathcal{S}_{(i-m+s,j-n+t)(i,j)}} \left\{ \begin{array}{l} \nabla\Psi_{(i-m+s,j-n+t)}(\mathbf{x}) \\ \quad \times\ (x_{i-m+s} - x_i)(y_{j-n+t} - y) \end{array} \right\} d\Omega \\
&= \sum_{(m,n)\in\mathcal{S}_{(i+m,j+n)(i,j)}} \int_{\Omega_{(i-m)(j-n)}} \sum_{(s,t)\in\mathcal{S}_{(i+s,j+t)(i+m,j+n)}} \\
&\quad \times \left\{ \begin{array}{l} \nabla\Psi_{(i+m,j+n)}(x + x_{i+m} - x_i, y + y_{j+n} - y_j) \\ \quad \cdot\ \nabla\Psi_{(i+s,j+t)}(x + x_{i+m} - x_i, y + y_{j+n} - y_j) \\ \quad \times\ (x_{i-m+s} - x_i)(y_{j-n+t} - y + y_{j+n} - y_j) \end{array} \right\} d\Omega \\
&= \int_{\Omega_{(i,j)}} \sum_{(s,t)\in\mathcal{S}_{(i+s,j+t)(i,j)}} \left\{ \begin{array}{l} \underbrace{\sum_{(i+m,j+n)\in\mathcal{G}_{(i+m,j+n)}} \nabla\Psi_{(i+m,j+n)}(\mathbf{x})(x_{i+s} - x_{i+m})}_{\{-1\ 0\}^T} \\ \quad \cdot\ \nabla\Psi_{(i+s,j+t)}(\mathbf{x})(y_{j+t} - y) \end{array} \right\} d\Omega \\
&= -\int_{\Omega_{(i,j)}} \underbrace{\sum_{(i+s,j+t)\in\mathcal{G}_{(i+s,j+t)}} \Psi_{(i+s,j+t),x}(\mathbf{x})(y_{j+t} - y)}_{0}\, d\Omega \\
&= 0, \qquad \text{(B.18)}
\end{aligned}$$

$$\begin{aligned}
\mathcal{R}_2 &= \int_\Omega \nabla\Psi_I(\mathbf{x}) \cdot \underbrace{\sum_{J\in\mathcal{G}_J} \nabla\Psi_J(\mathbf{x})(x_J - x_I)}_{\{1\ 0\}^T} (y - y_I)d\Omega \\
&= \int_\Omega \Psi_{I,x}(\mathbf{x})(y_I - y)d\Omega \\
&= \sum_{(m,n)\in\mathcal{S}_{(i+m,j+n)(i,j)}} \int_{\Omega_{(i-m,j-n)}} \Psi_{(i+m,j+n),x} \\
&\quad \times (x + x_{i+m} - x_i, y + y_{j+n} - y_j)(y - y_j)d\Omega \\
&= \int_{\Omega_{(i,j)}} \underbrace{\sum_{(i+m,j+n)\in\mathcal{G}_{(i+m,j+n)}} \Psi_{(i+m,j+n),x}(\mathbf{x})(y - y_j)}_{0}\, d\Omega \\
&= 0. \qquad \text{(B.19)}
\end{aligned}$$

Thus we have $\mathcal{H}_2 = 0$.

Finally, substituting Eqs. (B.14), (B.15) and (B.16) into Eq. (B.8) yields the relationship given by Eq. (57):

$$\begin{aligned}\int_{\Omega} \nabla\Psi_I(\mathbf{x}) \cdot \sum_{J\in\mathcal{G}_J} \nabla\Psi_J(\mathbf{x})[(x_J - x_I)\cos\theta + (y_J - y_I)\sin\theta]^2 d\Omega \\ = -2h_x h_y \cos^2\theta - 2h_x h_y \sin^2\theta \\ = -2h_x h_y. \end{aligned} \tag{B.20}$$

References

1. T. J. R. Hughes, *The Finite Element Method: Linear Static and Dynamic Finite Element Analysis* (Dover Publications, Mineola, New York, 2000).
2. C. A. Brebbia, J. C. F. Telles and L. C. Wrobel, *Boundary Element Techniques: Theory and Applications in Engineering* (Springer-Verlag, New York, 2012).
3. T. Belytschko, Y. Y. Lu and L. Gu, Element-free Gakerkin methods, *Int. J. Numer. Methods Eng.* **37** (1994) 229–256.
4. T. Belytschko, Y. Kronggauz, D. Organ, M. Fleming and P. Krysl, Meshless methods: An overview and recent developments, *Comp. Methods Appl. Mech. Eng.* **139** (1996) 3–47.
5. W. K. Liu, S. Jun and Y. F. Zhang, Reproducing kernel particle methods, *Int. J. Numer. Methods Fluids* **20** (1995) 1081–1106.
6. J. S. Chen, C. Pan, C. T. Wu and W. K. Liu, Reproducing kernel particle methods for large deformation analysis of nonlinear structures, *Comp. Methods Appl. Mech. Eng.* **139** (1996) 195–227.
7. S. N. Atluri and S. P. Shen, *The Meshless Local Petrov–Galerkin Method* (Tech Science Press, Forsyth, 2002).
8. X. Zhang and Y. Liu, *Meshless Methods* (Tsinghua University Press & Springer-Verlag, Beijing, 2004).
9. S. Li and W. K. Liu, *Meshfree Particle Methods* (Springer-Verlag, New York, 2004).
10. G. R. Liu, *Meshfree Methods: Moving Beyond The Finite Element Method*, 2nd edn. (CRC Press, Boca Raton, 2009).
11. D. Wang and P. Chen, Quasi-convex reproducing kernel meshfree method, *Comput. Mech.* **54** (2014) 689–709.
12. P. Metsis, N. Lantzounis and M. Papadrakakis, A new hierarchical partition of unity formulation of EFG meshless methods, *Comp. Methods Appl. Mech. Eng.* **283** (2015) 782–805.
13. J. Yang, P. Guan and C. Fan, Solving inverse Laplace equation with singularity by weighted reproducing kernel collocation method, *Int. J. Appl. Mech.* **9** (2017) 1750065.
14. Y. Guo and G. Yagawa, A meshless method with conforming and nonconforming subdomains, *Int. J. Numer. Methods Eng.* **110** (2017) 826–841.
15. C. T. Wu, Y. Wu, J. E. Crawford and J. M. Magallanes, Three-dimensional concrete impact and penetration simulations using the smoothed particle Galerkin method, *Int. J. Impact Eng.* **106** (2017) 1–17.
16. E. Yreux and J. S. Chen, A quasi-linear reproducing kernel particle method, *Int. J. Numer. Methods Eng.* **109** (2017) 1045–1064.
17. J. S. Chen, M. Hillman and S. W. Chi, Meshfree methods: Progress made after 20 years, *J. Eng. Mech.-ASCE* **143** (2017) 04017001.
18. W. K. Liu, S. Jun, S. Li, J. Adee and T. Belytschko, Reproducing kernel particle methods for structural dynamics, *Int. J. Numer. Methods Eng.* **38** (1995) 1655–1679.

19. G. R. Liu and Y. T. Gu, A local radial point interpolation method (LRPIM) for free vibration analyses of 2-D solids, *J. Sound Vib.* **246** (2001) 29–46.
20. J. X. Zhou, H. Y. Zhang and L. Zhang, Reproducing kernel particle method for free and forced vibration analysis, *J. Sound Vib.* **279** (2005) 389–402.
21. J. T. Chen, I. L. Chen, K. H. Chen, Y. T. Lee and Y. T. Yeh, A meshless method for free vibration analysis of circular and rectangular clamped plates using radial basis function, *Eng. Anal. Bound. Elem.* **28** (2004) 535–545.
22. L. Liu, L. Chua and D. Ghista, Mesh-free radial basis function method for static, free vibration and buckling analysis of shear deformable composite laminates, *Compos. Struct.* **78** (2007) 58–69.
23. D. Wang and Z. Lin, Free vibration analysis of thin plates using Hermite reproducing kernel Galerkin meshfree method with sub-domain stabilized conforming integration, *Comput. Mech.* **46** (2010) 703–719.
24. T. Bui, M. Nguyen and C. Zhang, A moving Kriging interpolation-based element-free Galerkin method for structural dynamic analysis, *Comp. Methods Appl. Mech. Eng.* **200** (2011) 1354–1366.
25. L. X. Peng, S. T. Yan, G. K. Mo and X. Zhang, Free vibration analysis of corrugated-core sandwich plates using a meshfree Galerkin method based on the first-order shear deformation theory, *Int. J. Mech. Sci.* **78** (2014) 8–18.
26. H. Zhang, J. Wu and D. Wang, Free vibration analysis of cracked thin plates by quasi-convex coupled isogeometric-meshfree method, *Front. Struct. Civil Eng.* **9** (2015) 405–419.
27. A. Soltanimaleki, M. Foroutan and J. Alihemmati, Free vibration analysis of functionally graded fiber reinforced cylindrical panels by a three dimensional mesh-free model, *J. Vib. Control* **22** (2016) 4087–4098.
28. M. Christon and T. Voth, Results of von Neumann analyses for reproducing kernel semi-discretizations, *Int. J. Numer. Methods Eng.* **47** (2000) 1285–1301.
29. Y. You, J. S. Chen and T. Voth, Characteristics of semi-and full discretization of stabilized Galerkin meshfree method, *Finite Elem. Anal. Des.* **38** (2002) 999–1012.
30. D. Wang and Z. Lin, Dispersion and transient analyses of Hermite reproducing kernel Galerkin meshfree method with sub-domain stabilized conforming integration for thin beam and plate structures, *Comput. Mech.* **48** (2011) 47–63.
31. D. Wang and Z. Lin, A comparative study on the dispersion properties of HRK and RK meshfree approximations for Kirchhoff plate problem, *Int. J. Comput. Methods* **9** (2012) 1240015.
32. G. L. Goudreau and R. L. Taylor, Evaluation of numerical integration methods in elastodynamics, *Comp. Methods Appl. Mech. Eng.* **2** (1973) 69–97.
33. T. Belytschko and R. Mullen, On dispersive properties of finite element solutions, in *Modern Problems in Elastic Wave Propagation*, eds. J. Miklowitz and J. Achenbach (Wiley, New York, 1978), pp. 67–82.
34. K. Kim, A review of mass matrices for eigenproblems, *Comp. Struct.* **46** (1993) 1041–1048.
35. I. Fried and M. Chavez, Superaccurate finite element eigenvalue computation, *J. Sound Vib.* **275** (2004) 415–422.
36. C. A. Felippa, Construction of customized mass-stiffness pairs using templates, *J. Aerosp. Eng.* **19** (2006) 241–258.
37. C. A. Felippa, Q. Guo and K. C. Park, Mass matrix templates: General description and 1D examples, *Arch. Comput. Methods Eng.* **22** (2015) 1–65.

38. D. Wang, X. Li and F. Pan, A unified quadrature-based superconvergent finite element formulation for eigenvalue computation of wave equations, *Comput. Mech.* **59** (2017) 37–72.
39. D. Wang, W. Liu and H. Zhang, Novel higher order mass matrices for isogeometric structural vibration analysis, *Comp. Methods Appl. Mech. Eng.* **260** (2013) 92–108.
40. D. Wang, X. Li, W. Liu and H. Zhang, An ultra-accurate dynamic isogeometric analysis with higher order mass formulation, *Sci. China-Technol. Sci.* **57** (2014) 1293–1309.
41. D. Wang, W. Liu and H. Zhang, Superconvergent isogeometric free vibration analysis of Euler–Bernoulli beams and Kirchhoff plates with new higher order mass matrices, *Comp. Methods Appl. Mech. Eng.* **286** (2015) 230–267.
42. D. Wang, Q. Liang and H. Zhang, A superconvergent isogeometric formulation for eigenvalue computation of three dimensional wave equation, *Comput. Mech.* **57** (2016) 1037–1060.
43. D. Wang, Q. Liang and J. Wu, A quadrature-based superconvergent isogeometric frequency analysis with macro-integration cells and quadratic splines, *Comp. Methods Appl. Mech. Eng.* **320** (2017) 712–744.
44. J. Dolbow and T. Belytschko, Numerical integration of the Galerkin weak form in meshfree methods, *Comput. Mech.* **23** (1999) 219–230.
45. J. S. Chen, C. T. Wu, S. Yoon and Y. You, A stabilized conforming nodal integration for Galerkin meshfree methods, *Int. J. Numer. Methods Eng.* **50** (2001) 435–466.
46. T. P. Fries and T. Belytschko, Convergence and stabilization of stress-point integration in mesh-free and particle methods, *Int. J. Numer. Methods Eng.* **74** (2008) 1067–1087.
47. J. S. Chen, M. Hillman and M. Rüter, An arbitrary order variationally consistent integration for Galerkin meshfree methods, *Int. J. Numer. Methods Eng.* **95** (2013) 387–418.
48. D. Wang and J. S. Chen, A Hermite reproducing kernel approximation for thin-plate analysis with sub-domain stabilized conforming integration, *Int. J. Numer. Methods Eng.* **74** (2008) 368–390.
49. D. Wang and H. Peng, A Hermite reproducing kernel Galerkin meshfree approach for buckling analysis of thin plates, *Comput. Mech.* **51** (2013) 1013–1029.
50. D. Wang, C. Song and H. Peng, A circumferentially enhanced Hermite reproducing kernel meshfree method for buckling analysis of Kirchhoff–Love cylindrical shells, *Int. J. Struct. Stab. Dyn.* **15** (2015) 1450090.
51. D. Wang, M. Sun and P. Xie, A boundary enhancement for the stabilized conforming nodal integration of Galerkin meshfree methods, *Int. J. Comput. Methods* **12** (2015) 1550009.
52. D. Wang and J. Wu, An efficient nesting sub-domain gradient smoothing integration algorithm with quadratic exactness for Galerkin meshfree methods, *Comp. Methods Appl. Mech. Eng.* **298** (2016) 485–519.
53. B. Dong, C. Li, D. Wang and C. T. Wu, Consistent multiscale analysis of heterogeneous thin plates with smoothed quadratic Hermite triangular elements, *Int. J. Mech. Mater. Des.* **12** (2016) 539–562.
54. C. T. Wu, S. W. Chi, M. Koishi and Y. Wu, Strain gradient stabilization with dual stress points for the meshfree nodal integration method in inelastic analyses, *Int. J. Numer. Methods Eng.* **107** (2016) 3–30.
55. B. Wang, Q. Duan, Y. Shao, X. Li, D. Yang and H. Zhang, An efficient nodal integration with quadratic exactness for three-dimensional meshfree Galerkin methods, *Eng. Anal. Bound. Elem.* **70** (2016) 99–113.
56. M. Hillman and J. S. Chen, An accelerated, convergent, and stable nodal integration in Galerkin meshfree methods for linear and nonlinear mechanics, *Int. J. Numer. Methods Eng.* **107** (2016) 603–630.